ICFA INSTRUMENTATION BULLETIN*

The publication of the ICFA Instrumentation Bulletin is an activity of the Panel on Future Innovation and Development of ICFA (International Committee for Future Accelerators).

Volume 19

• Fall 1999 Issue

ICFA INSTRUMENTATION BULLETIN

The publication of the ICFA Instrumentation Bulletin is an activity of the Panel on Future Innovation and Development of ICFA (International Committee for Future Accelerators). The Bulletin reports on research and progress in the field of instrumentation with emphasis on application in the field of high-energy physics. It encourages issues of generic instrumentation.

The views expressed in this Bulletin do not necessarily represent those of the ICFA Panel or the editor. In all cases, the authors are responsible for their manuscripts. The printed version is mailed out in limited numbers to institutions on the SLAC Instrumentation mailing list. Issues of the ICFA Instrumentation Bulletin are accessible electronically on our Web site:

http://www.slac.stanford.edu/pubs/icfa/

Cover: The illustration depicts L. J. Waghenaer's marine atlas, "The Mariner's Mirror," published in 1588. Lucas Janszoon Waghenaer was born in Holland in the 1530s. He became a famous ship pilot in his time. In 1584, he published the atlas ("Spieghel der Zeevaerdt") which was greatly valued among mariners for centuries. This was not due only to the map content, but also to the detailed knowledge of navigation techniques of that time. The atlas, as it appears on our page, is the same one used for the Dutch to English translation.

Conference List

- Frontier Detectors for Frontier Physics, 8-th Pisa Meeting on Advanced Detectors, La Biodola, Isola d'Elba, May 21-27, 2000.

- IMAGING 2000, Royal Institute of Technology, Stockholm, Sweden, June 28-July 1, 2000.

- IEEE Nuclear Science Symposium and Medical Imaging Conference, Lyon, France, October 15-20, 2000

- RICH 2001 Workshop, Pylos, Greece, September 3-7, 2001.

Table of Contents

MICROMEGAS: Results and Prospects

I. Giomataris

CEA/Saclay, DAPNIA,#91191 Gif-sur-Yvette Cedex, France

Introduction

A lot of effort has been invested in the development of the Microstrip Gas Chamber (MSGC) [2] to be used as tracker for the LHC project. This technique allows good localization accuracy and double track resolution. However, it is necessary to operate it with a relatively low gas gain because of the presence of the insulator near the amplification region and the fragility of the structure.

Recently, a new preamplification structure called GEM [3] has been introduced, which can give additional gas gain and compensates for the lack of gain in the original MSGC. Other concepts of novel proportional counters have been recently proposed: CAT [4] and MICRO-DOT [5]. A review of recently developed gaseous detectors can be found in Reference [6].

MICROMEGAS [1] is a high-gain gaseous detector, which is a stand-alone detector without a need for additional preamplification. It combines high accuracy, high-rate capability, excellent timing properties, and robustness. These results were confirmed by a similar structure having a wider amplification gap and a thicker metallic grid [7].
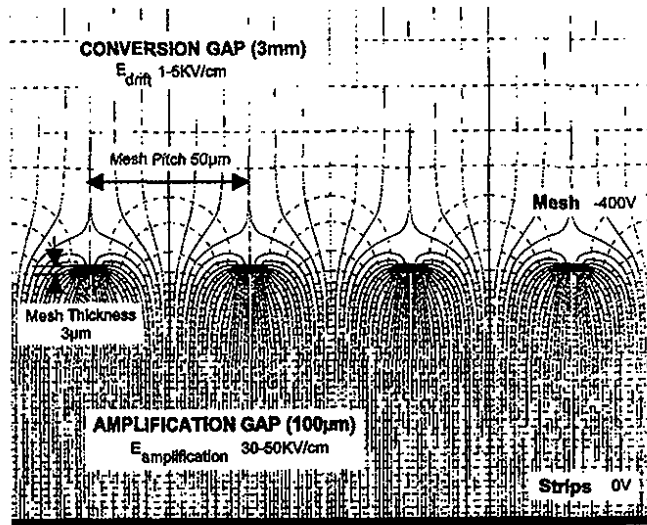

Figure 1. Map of the electric field lines around the micromesh (50 μm step, 37 μm diameter of the openings).

1. Detector Description

A detailed description of MICROMEGAS is given in References 1,8,9. The detector has a two-stage parallel plate avalanche chamber that has a narrow amplification gap defined by the anode plane and a cathode plane made by a Ni electroformed micromesh. Several 15x15 cm^2 chambers with a conversion gap of 3 mm, an amplification gap of 100 or 50 μm with a strip pitch of 317.5 μm, have been designed and fabricated. The parallelism between the micromesh grid and the anode is maintained by spacers of 150 μm in diameter, and placed every 2 mm. They are printed on a thin epoxy substrate by conventional lithography of a photoresistive polyamide film. The thickness of the film defines the amplification gap. This is a cheap and simple process that allows the construction of large detectors with excellent uniformity (10%) and an energy resolution over the whole surface.

1. Electric Field Configuration

The knowledge of the shape of the electric field lines close to the micromesh is a key issue for an optimal operation of the detector and especially for an efficient transfer of electrons to the amplification gap. The electric field is homogeneous in both the conversion and the amplification gap. It exhibits a funnel like shape around the openings of the microgrid: field lines are highly compressed towards the middle of the openings, into a small pathway equal to a few microns in diameter. The compression factor is directly proportional to the ratio of the electric fields between the two gaps. Figure 1 displays details of the field lines near the grid used in the present test (50 μm opening pitch).

The electrons liberated in the conversion gap by the ionizing radiation follow the electric field lines and are focused into the multiplication gap where the amplification process takes place. The ratio between the electric field in the amplification gap, and that of the conversion gap must be set at large values (>5) to permit full electron transmission, and to partially reduce ion cloud produced in the avalanche, to escape into the conversion gap.
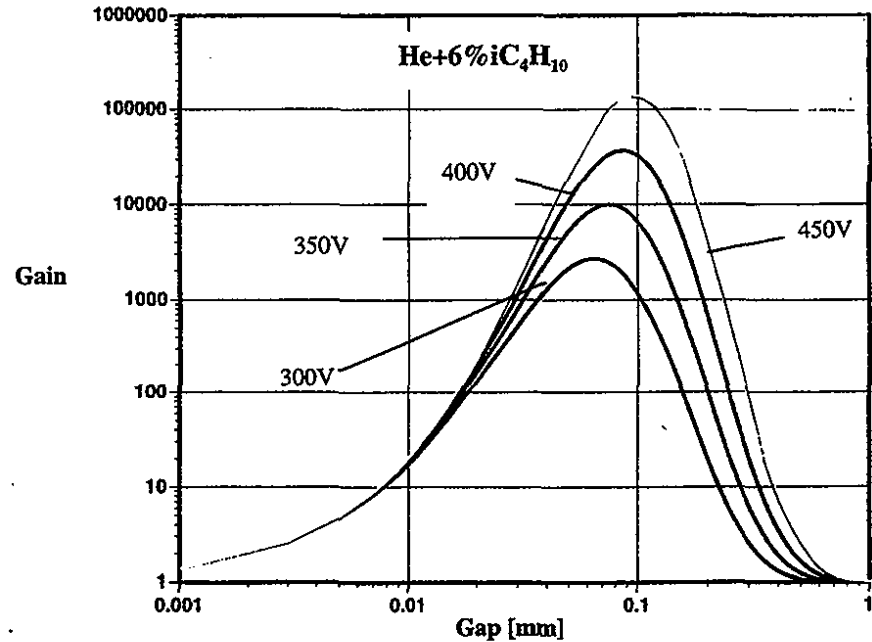

Figure 2. Calculated gas gain in He + 6% Isobutane as a function of the amplification gap for various potentials applied on the microgrid.

2. Advantage of the Small gap

An interesting property of the MICROMEGAS is that, given its narrow gap, localized small variations of the amplification gap, due to mechanical defects, do not induce gain fluctuation; they are compensated by an inverse variation of the amplification coefficient. This behavior can be theoretically explained as:

The electron multiplication (M) in the uniform electric field between two parallel plates in a gas at a pressure p, is described by:

$$M = e^{ad} \qquad (1)$$

Where d is the gap of the two parallel electrodes and a is the 1-st Townsend coefficient, which represents the mean free path of the electron between two ionizations. A good approximation of this coefficient is given by Rose and Korff formula:

$$a = p A e^{-Bp/E} \qquad , \qquad (2)$$

where E is the electric field and A, B are parameters depending on the gas mixture.

At high electric field values of the 1-st Townsend coefficient saturates because its value approaches the mean free path given by the inelastic collision cross-section. The electric field is E = V/d where V is the applied voltage. By substituting equation (2) in (1) we get:

$$Log(M) = A p d e^{-Bpd/V} \qquad . \qquad (3)$$

The multiplication factor M is a function of the quantity pd. Figure 2 shows M as a function of the gap (d) for a typical mixture of Ar + 5% DME, and for V=300, 350 and 400 Volts at 1 bar.

One can see that M rises as d increases. It reaches a maximum and then falls at large values of d. The maximum is obtained by a differentiation of equation (3), resulting in $\Delta M/M = ad(1- Bd/V)$. The maximum value is obtained for a value d = V/B at p =1 bar. The amplification gap, chosen in this way, depends slightly on the gas mixture. For a given applied potential, the multiplication factor is at maximum in the range of gaps between 30-100 microns. This is the range currently used by the MICROMEGAS detectors. In this range the multiplication factor is maximized, and fluctuations due to defects of flatness of the two parallel electrodes are canceled. In few words such narrow gaps are ideal for an optimal operation of the parallel plate gaseous detectors, since all fluctuations are suppressed, due to mechanical defects, atmospheric pressure, or temperature variations.

It is quite difficult to verify experimentally the previous calculation, as a large variety of very narrow gaps are needed. It needs to be pointed out that this has been verified for two gaps (d=100 and 50 µm), but further work is needed to complete the study. It is much easier to verify the variation of M with pressure, which is expected to be equivalent to the gap variation.

Figure 3 shows the multiplication factor obtained from our measurements as a function of pressure for He + 6% Isobutane for a gap of 50 microns.
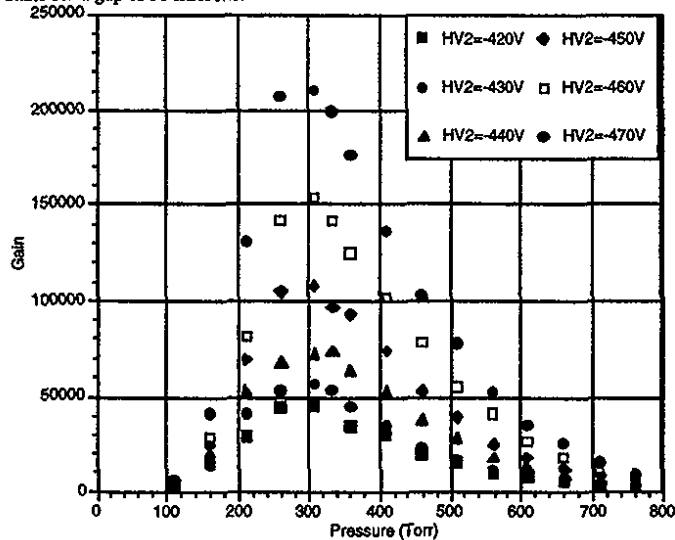

Figure 3. Measured gain in He + 6% Isobutane as a function of the gas pressure for various potentials applied on the micro-grid.

The curve clearly shows that there is a maximum multiplication at p = 500mbar. Notice that the optimal operation of a conventional parallel plate avalanche chamber (d≈4 mm) is at pressures of the order of 10 mbar.

3. Gain Properties

A high gas gain in a gaseous detector is a key issue for many applications. In particular, a detection of minimum ionizing particles requires a large dynamic range because of the Landau fluctuation of the deposited energy and the emission of heavy ionizing particles. The goal of a "good" detector is to achieve a stable operation before a breakdown, which corresponds to a total charge per avalanche approaching 10^7-10^8 (so-called Rather limit).

MICROMEGAS have been tested with a large variety of gas mixtures. Results have been published for Argon mixtures with various hydrocarbons [8,9]; the maximum safe gain is close to 10^5 with 5-10% of additional Isobutane, and three times higher with a small amount of Cyclohexane. Adding CF_4 to the previous mixtures is important, because it improves the time resolution and the total deposited energy [10]. Neon or He mixtures with hydrocarbons allow an increase of the total charge per single avalanche that approaches the highest Rather values (about 10^8).

Figure 4 shows the gas gain measured in He + 6% Isobutane mixture using single photoelectrons produced under UV illumination; the maximum gas gain reached was ~1.8 x 10^7.
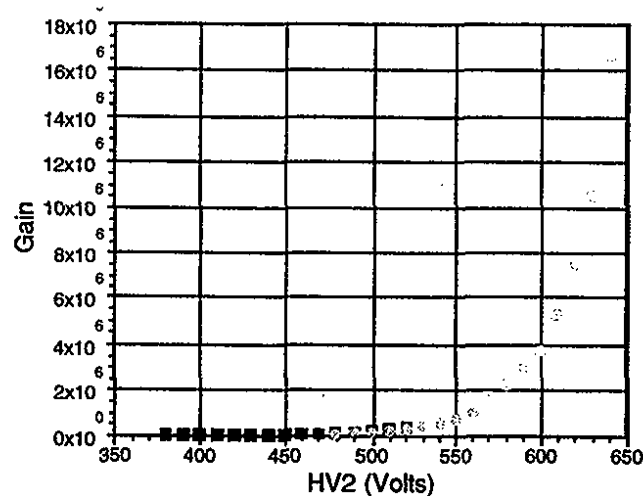

Figure 4. Gas gain measured in He + 6% Isobutane as a function of the applied potential.

Mixtures of high-Z gases, such as Krypton or Xenon, are relevant for many applications in X-ray digital radiography, crystallography, and synchrotron radiation studies. A lot of tests have been performed in our laboratory to optimize the operation of our detector, using such gas mixtures. The general conclusion is that the maximum achievable gas gain increases with heavier hydrocarbon quenchers and lower ionization potentials. For example, Figure 5 shows the gas gain measured as a function of the applied voltage and the various quenchers added to the Xenon carrier gas. The maximum achievable gas gain is increasing as one goes from the Isobutane (4500) to Cyclohexane (10^6), and finally to Cyclohexene (3.10^6). Such high gas gain gives the required margin factor when a detector has to cope with very-high X-ray environments, or at high-pressure operations.
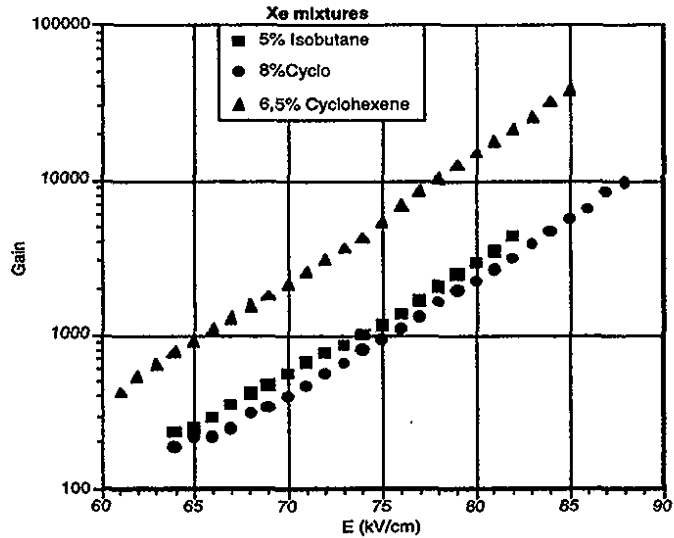
Figure 5. Gas gain measured in various Xe mixtures as a function of the applied potential.

6. Signal Development and Time Resolution

A signal induced on the anode strips is a sum of the electron and ion signal. The charge signal is mainly due to the positive ion drifting to the micromesh electrode, which takes place typically within 100ns, depending on the amplification gap and the gas mixture. Figure 6 shows the preamplifier response for an Argon + 10% Isobutane gas mixture and for various gaps. A reduction of the amplification gap from 100 to 50 microns reduces the signal risetime by a factor three. Using a gap of 30 μm the rise time is only 17ns, another reduction of a factor of two. So, in the latter case, the shaping of the signal around 17ns allows the fully induced charge to catch up, and therefore, permits a comfortable operation of the detector at moderate gains. One must also take into consideration that the ion collection time decreases by using higher ion mobility carrier gas (Ne or He).
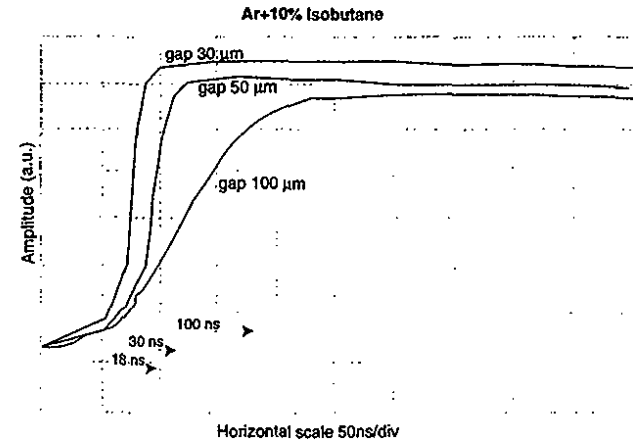

Figure 6. Signal provided by a charge preamplifier for various amplification gaps: 100, 50 and 25 μm.

The conclusion is that MICROMEGAS can be used with low-noise charge preamplifiers without loss due to ballistic deficit, which occur in other microstrip devices; choosing the right amplification and the right gas mixture, the rise of the detector can be compatible with the shaping of the charge amplifier. Due to the faster drift velocity, the electron current is larger and faster (about 1ns instead of 100ns for the ion signal). Therefore, a very fast rise of the signal, followed by a tail due to the ion drift, is expected. Such a fast electron signal is quite difficult to catch, but is within reach with present electronics. For example, using the current-sensitive preamplifier with a fast rise time (t<1 ns), the result is spectacular (see Figure 7).
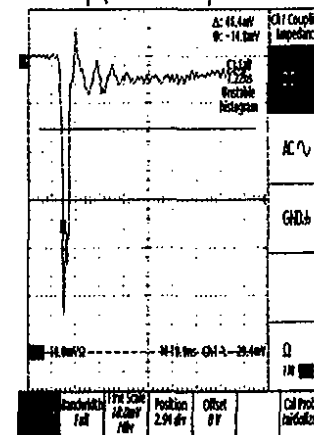

Figure 7. Fast electron signal from the current preamplifier in Ar + 10% Isobutane gas mixture. Notice that the electron signal and the ion tail are developed within 5 ns and 80 ns, respectively.

The fast signal has a rise of 1ns and an amplitude of ten times higher than the ion tail. Such fast signals will allow the development of novel drift chambers or small TCP's with a time resolution below 1ns.

The time resolution of MICROMEGAS was first investigated using the Lecroy-MQS104 preamplifier. The measurement showed that the time accuracy is dominated by the time-jitter of the ionization clusters produced by the minimum ionizing particles traversing the conversion gap. The best result (4.5ns) was obtained with a high-drift velocity gas: a mixture of Argon, CF_4, and Isobutane. It is, therefore, quite logical to speculate that using CF_4 as a carrier gas with a conversion depth of 1 mm and faster electronics, one can reach a time accuracy of 1ns.

7. Space Resolution

Several groups, using various detector configurations, in terms of pitch, amplification gap, and operating gas have investigated the space resolution. The results obtained are already published and are summarized in Table I.

The Saclay group has initially tested detectors having 317 micron pitch [8]. Accuracy of 60 μm has been measured using an Argon + DME mixture [9]. Recent results with small pitch detectors (50 and 100 μm) gave a spatial resolution of 25 μm with a mixture of He + 20 % DME, and 12 μm with a mixture of CF_4 and 20% Isobutane. The Subathec-Nantes group, using a 200 μm pitch, has measured an accuracy of 45 μm [6]. A comparable result has been obtained by the Mulhouse group using a Ne+ 10% DME gas.

The conclusion is that the accuracy of MICROMEGAS can satisfy the needs of most of the high-energy experiments for tracking purposes. Moreover, using narrow strips and low-diffusion gas fillings, the spatial resolution is closed to that of the silicon micro-strip detector. One can speculate that MICROMEGAS can be used as a micro-vertex detector close to the interaction region of particle colliders with several advantages over the silicon detector: higher radiation resistance, lower cost and lower material budget.

Table I
Resolution MICROMEGAS

σ (μm)	PITCH (μm)	Gas mixture	Institute
80	317	Ar+10% iC_4H_{10}	Saclay
60	317	Ar+10% DME	Saclay
45	200	Ar+25% CO_2	Subatech
		Ne+10% DME	UNI-Mulhouse
24	50	He+10% DME	Saclay
12	100	CF_4+20% iC_4H_{10}	

8. Rate Capability and Comparison with Other Detectors

Many tests have shown that the rate capability of the gaseous detectors strongly depends on the type of the incident particle beam being used. Two particular cases will be distinguished.

8.1. Rate Capability with X-ray Particles

This environment is relevant for applications in the medical field. Detailed results with various mixtures and various fluxes are presented in Reference 11. We have observed that gas gain does not saturate with rate, up to fluxes of 10^9/mm/s. Systematic studies in the laboratory show that the maximum achievable gas gain decreases with the flux. At a flux of 10^7/mm^2/s and X-rays of 8 keV energy, the gas gain is higher than 10^3, which allows full detection efficiency.

8.2. Rate Capability with Charged Particles

Investigations, using high flux of incident beta particles, low-energy protons or high-energy muons, have shown that the detector has a similar behavior to that of the X-rays, i.e., MICROMEGAS can cope with very high rates of these particles. However, an undesirable effect has been observed when the incident beam is composed by high-energy hadrons and when a high discharge rates are proportional to the incident hadron flux.

It is believed that large ionization deposits trigger discharges. These deposits are probably released by recoil nuclei produced by charged particles, especially hadrons traversing the detector. As ionization losses are proportional to z^2, the recoil nuclei resulted from elastic or quasi-elastic interactions, with energy in the MeV region, are quite efficient to produce heavy ionization in the gas. A typical example is a nuclear interaction on the Argon nuclei producing fully ionized Argon nuclei, while having a 1 MeV kinetic energy. The whole energy

will be lost within 100 microns producing about 10^5 electron-ion pairs in the conversion gap. This enormous quantity of charges is again multiplied by the detector gain in the amplification gap, exceeding the "Rather" limit (a few 10^7), thus triggering a breakdown. Taking into account the nuclear collision length for hadrons, which is about 10^4 cm in Argon, the probability to produce such process in the conversion gap is of the order of 10^{-6}. This spark probability produces a serious limitation when the detector has to deal with very high hadron flux.

In the case of muons, the corresponding cross section is several orders of magnitudes lower; therefore, the probability to induce sparks is negligible. MICROMEGAS has been tested with ~5 x 10^7 muons in a small area (a few cm^2) without serious losses of its performance.

It is quite important to note that in MICROMEGAS the induced sparks are not propagating in the whole area of the detector, instead they are limited in an area of maximum a few mm^2, and the duration of this phenomena doesn't exceed 100ns. There are possible consequences where the discharges vary from a dead time to a destruction of the electronics, or even the detector itself.

Dead time

As it has been already mentioned, the discharges are local and have very low duration in MICROMEGAS. Large RC charging circuits, which can produce significant dead times, have to be avoided.

Destruction of the Electronics

Several protections have been tested: protecting diodes, a small resistor or an appropriate capacitor, between the anode strip and the front-end chip, can prevent damage of the electronics.

Destruction of the Detector

This is a serious problem in delicate micro-strip detectors. For example, MSGC detectors are easily damaged by the sparks, because of the presence of the insulator and thin delicate anode strips surrounded by a region of a strong electric field. Adding a preamplification stage, using, for example, a GEM structure, provides additional safety to the MSGC. However, GEM itself suffers of high capacitance, large stored charge that is dangerous when it is released. The released charge is again multiplied in the second amplification structure that can be damaged. Moreover the GEM structure consisting of millions of individual multipliers is quite delicate; any short-circuit due to defects or discharges is not tolerable. In both cases, the sparking rate must be reduced to a very low level.

In comparison, MICROMEGAS is extremely robust; the detector has been tested with a sparking rate of 1000 sparks/s in small 1 mm^2 area. After a total accumulated number of sparks of 10^7/mm^2; the detector was still alive without any loss to its performance.

9. Radiation Resistance

Parallel plate detectors exhibit high radiation resistance. The electric field is homogeneous over the whole amplification gap and accumulation of undesirable effects, like polymerization during the avalanche process, has very little effect. The radiation resistance of the detector has been tested in the laboratory using an intense X-ray generator. With a gas mixture of Argon + 6% Isobutane, the gas gain of the detector remained stable up to a total accumulated charge of 18.3 mC/mm^2, which corresponds to about 10 years of LHC operation at the full luminosity, and at 40 cm from the interaction point [11].

10. New Developments

2. Two-dimension Read-out

In High-Energy experiments, the two-dimension read-out is usually not in crucial demand, because the tracking of charged particles can be performed using several X-Y planes. In some medical applications, employing, for instance, the scanner technique, one-dimensional read-out is usually sufficient. For example, anode strips pointing to the X-ray source can be used.

In some applications, however, the two-dimensional read-out is mandatory. A straightforward method is to use the anode pads. Any pad size is compatible with MICROMEGAS, but a careful study of the implementation of the electronic chain is required. A possible drawback is the increase in the number of the read-out channels, especially when high accuracy is required. In order to decrease the number of electronic channels, a second plane consisting of strips perpendicular to the anode strips, is required. Several solutions are presently under

investigation. For example, the Nantes group has investigated a solution based on strips printed on a thin 50 micron FR4 insulator on the backplane [12]. These strips are perpendicular to the anode strips that are printed on the upper side of the insulator. A first attempt has shown a quite important suppression of the pick-up signal on the second strip plane. A second study used the resistive anode strips and the charge division method. Recent results obtained in a particle beam are promising. Our group is pursuing a novel way to resolve this problem using micromesh made of strips. The first results are encouraging.

3. Photo-detector

The first idea is to benefit, as it has been already discussed, from the very high gas gain obtained with He-based gas mixtures. Such mixtures have a low sensitivity to the ionizing particles and are ideal for the photon counting.

The second idea is the design of a special configuration of the photocathode, deposited on top of the metallic grid of MICROMEGAS, that will allow achieving high gas gains, and at the same time fully suppressing the dangerous effect of photon feedback. The first results are encouraging; the detection efficiency of single electrons is close to 100%, and the time resolution in the sub-nanosecond range [13] is below 1ns.

4. Micro-TPC

The idea of a Micro-TPC has been mentioned in the last Vienna Conference [14]. It is a new concept of a TPC-like structure, surrounding the beam pipe, and mounted very close (about 1 cm) from the interaction point of a particle collider. The MICROMEGAS detector covers the two end plates of the TPC and has fine anode pads (about 200 micron) as read-out elements.

A sketch of the micro-TPC is shown in Figure 8. It illustrates a cylindrical TPC with a 10 mm internal radius, 30 mm external radius, and a length of 80 mm.
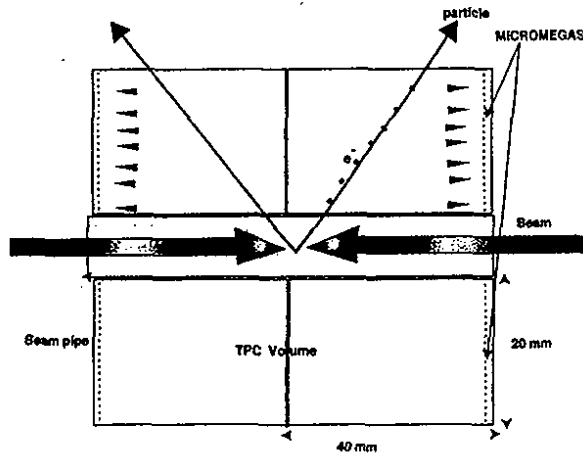

Figure 8. A schematic concept of the micro-TPC structure, read-out by a MICROMEGAS micro-pad detector.

The total drift length is 40 mm which corresponds to a maximum drift time of 32ns for CF_4 gas mixture or about 100ns for slower gas fillings (i.e., He mixtures). With a low diffusion gas mixture, crude calculations show that the spatial resolution per each detected point should be about 20 micron in the end plate and 100 microns in the middle of the TPC. Taking into account the large number of detected clusters (about 100) a mean accuracy of a few microns is expected.

Such performance exceeds by far that of the Silicon detector, where the spatial resolution is limited by the multiple scattering effect occurring in the material of the semiconductor. Moreover the high radiation resistance of MICROMEGAS offers the possibility to install the structure close to the beam pipe (in a more challenging configuration, the beam pipe is placed inside), in order to improve the impact parameter resolution.

This is a good challenge for the B-meson tagging and the particle identification. Examples of possible applications are the electron colliders, especially those dedicated to B-physics. The idea can be extended to other accelerators, including the very-high luminosity hadron machines.

11. Applications

The high counting rate, the excellent time resolution, and the high accuracy of MICROMEGAS combined with its low cost, radiation resistance and robustness, offer a lot of potential applications in high energy physics, as well as in the X-ray imaging. We now present several examples.

11.1. COMPASS

COMPAS is a new fixed-target experiment [15], recently approved by the CERN-SPS committee, with the main objective of measuring gluon polarization inside the nucleus. It uses a large 40x40 cm^2 MICROMEGAS detector for the upstream tracking (SAT) system.

For that purpose, special electronics has been developed by the Saclay COMPASS-group, based on the low-noise charge preamplifier – discriminator followed by a multi-hit TDC. The detector equipped with the new electronics is actually under test. First results are promising.

11.2. HELLAZ

The aim of the HELIAZ experiment is to measure the energy spectrum of the solar neutrinos in the low-energy range, and in particular, the p-p neutrino emission, while employing a high-pressure He TPC volume. Such measurement is important to clarify the puzzle that arises from present results made at higher neutrino energy, since only 50% of the neutrino flux predicted by the standard solar model reaches earth.

The idea is to fully reconstruct the recoil electron produced by the elastic scattering of the incident neutrino with He gas. Using the kinematics and assuming the neutrino direction (from the sun) one can then evaluate the neutrino energy.

A major experimental deal is to detect the ionization cloud produced by the electron from the primary interaction. For that, a challenging time resolution is required in order to detect single electrons close in time ($\sigma_t < 10ns$). Using a small MICROMEGAS prototype and He mixture, the College de France group, has achieved the required performance [16].

11.3. TOF

TOF is an European collaboration for high-resolution measurements of neutron cross section [17], for both fission and capture reaction between 1 eV to 250 MeV. MICROMEGAS is proposed for two purposes :
1) Neutron detection based on the ionization produced by the 3He(n,p)T reaction using a standard MICROMEGAS with a gas mixture of 3He and CF_4. The idea is to measure the beam profile and monitor the neutron fluence.
2) MICROMEGAS is used as a photodetector with CsI coating to readout the fast component of BaF_2 scintillation light emitted around 190nm. At that wavelength the quantum efficiency of the CsI is ~15%.
The objective is to measure the multiplicity of the gammas produced by a neutron in the range of 1–8MeV. The excellent time resolution of MICROMEGAS (1ns) is of great importance in order to reject accidentals and other backgrounds.

11.4. TESLA

The use of MICROMEGAS for the future linear collider (TESLA) experiment [18] is under study by a group of Saclay physicists. The idea is to design a pad detector, placed at the end plate of the drift volume of a central TPC in order to improve its performance and reduce the ion build-up which is a basic limitation in large drift volumes.

11.5. Medical and biological applications

Biological imaging studies, such as protein crystallography, using synchrotron radiation beams, are very demanding in terms of particle flux, accuracy, robustness, and fast read-out. These studies are often performed with soft X-rays [19,20] in the range of about 10keV. At higher X-ray energy, however, one needs either

heavier gas mixtures or high-pressure operation of the detector. The optimal use of the Xenon gas mixtures could be valuab

Another application of our detector is in medical radiology, where the trend is the digital read-out technology in order to replace the photographic film, with improved sensitivity and a spatial resolution comparable to the film. Beta radiography is employed in medical and biological investigations to image human or animal tissues labeled with beta-emitting radionucleides. One approach has found industrial applications consisting of using a multistep parallel-plate avalanche chamber coupled to an image intensifier and a CCD to read-out the UV light emitted during the avalanche development in the detector [21].

These are some examples of a large field of possible applications where the use of MICROMEGAS can simplify the construction and improve the performance in terms of accuracy and read-out speed. Table II summarizes the results obtained, as well as expected best performance.

Table II

	Measured	Ultimate
SPATIAL RESOLUTION μm (rms)	12 μm in CF_4	< 10
TIME RESOLUTION ns (rms)	4.5	< 1
ENERGY RESOLUTION at 5.9 keV (FWHM)	13%	13%
SIGNAL to NOISE for M.I.P's	> 100	> 100
RADIATION HARD (mC/mm²)	10 - 30 years of LHC	> 30
RISE TIME OF THE FAST SIGNAL (ns)	< 1	< 1

12. Conclusions

The main characteristics of a novel gaseous detector MICROMEGAS have been described. The measured performances of MICROMEGAS detector can be summarized as follows :

- High efficiency for minimum ionizing particles with large plateau has been measured.
- Spatial resolution of 12 μm has been achieved in CF_4 gas.
- A time resolution of 4.5 ns has been measured in a particle beam. Using fast current preamplifiers and CF_4 mixture, a time resolution of 1 ns is expected for minimum ionizing particle detection.
- The detector is able to cope with X-ray fluxes, as high as $10^7/mm^2/s$. Similar results are obtained when the ionization particles are electrons or muons. With high-energy hadron beam, however, a limitation

has been observed due to the production of highly ionizing particles inducing local breakdown. The detector is, however, radiation hard and can cope with a very large amount of such discharges, without significant dead time and damage to the electronics.

- A new photodetector using the MICROMEGAS structure was presented, giving excellent single electron efficiency (close to 100%) and time resolution below 500ps.
- A new micro-vertex, suitable to measure the impact parameter with an accuracy of a few microns, was proposed. It is called the micro-TPC and can surround the beam pipe close to the interaction point.
- The detector is suitable for many applications in physics or for high-rate imaging devices.

References

[1] Y. Giomataris, Ph. Rebourgeard, J.P. Robert, and G. Charpak, Nucl. Instr. Meth. A376(1996)29-35.
[2] A. Oed, Nucl. Instr. Meth. A263(1988)351.
[3] F. Sauli, Nucl. Instr. Meth. A386(1997)531.
[4] F. Bartol et al., J. Phys. III France 6(1996)337.
[5] S. Biagi et al., Nucl. Instr. Meth. A366(1995)76.
[6] F. Sauli, Nucl. Instr. Meth. A419(1998)189.
[7] A. Sarvestani et al., Nucl. Instr. Meth. A410(1997)238.
[8] G. Charpak et al., Nucl. Instr. Meth. A412(1998)47.
[9] G. Barrouch et al., Nucl. Instr. Meth. A423(1999)32.
[10] J. Va'vra et al., Nucl. Instr. Meth. A324(1993)113.
[11] G. Puill, J. Derre, I. Giomataris, and Ph.Rebourgeard, "MICROMEGAS: high-rate and radiation hardness results," submitted to the 1999 IEEE Conference, Seattle, Washington, U.S.A..
[12] J.P Cussonneau et al. , Nucl. Instr. Meth. A419(1998)452
[13] J. Derre, I. Giomataris, J.P.Perroud, and Ph. Rebourgeard et al, " Fast electron signals and single electron with MICROMEGAS photodetector" (in preparation).
[14] I. Giomataris, Nucl. Instr. Meth. A419(1998)239.
[15] COMPASS, CERN/SPSLC 96--14 SPLSLC/P297 and CERN/SPSLC 96--30 SPLSLC/P297.
[16] Ph. Gorodewski et al, 'Identification of solar neutrinos by individual electron counting in HELLAZ' submitted to the RICH 98 Conference, Ein Gedi, Israel.
[17] S. Abramowitch, et al., CERN/SPSC 99-8, SPSC/P 310, 17 March 1999.
[18] 'Linear collider: physics and detector studies," DESY 97-123E, December 1997.
[19] H.J. Besch, Nucl. Instr. Meth. A419(1998)202.
[20] B. Schmidt, Nucl. Instr. Meth. A419(1998)230.
[21] G. Charpak et al., Proc. Nat. Acad. Sci., Vol. 86, 1989, p. 1741.

A How-to Approach for a 3D-Simulation of Charge Transfer Characteristics in a Gas Electron Multiplier (GEM)

Archana SHARMA[1]

CERN, Geneva, Switzerland and GSI Darmstadt, Germany

Abstract

In this paper, a detailed description of how to simulate charge transfer processes in a gaseous device is presented, taking the Gas Electron Multiplier (GEM) as an example. A three-dimensional simulation of the electric field and avalanche is performed. Results on charge transport are compared to experiment, which agree within experimental errors; avalanche mechanism and positive ion feedback are also studied. The procedures used in the simulation are described in detail, and program scripts are appended.

1. Introduction

The simulation of the performance of gaseous detectors has been extensively developed in the last decade. The main tool to study the electrostatic properties of wire chambers, GARFIELD, has been extended into three-dimensions [1] with the inclusion of planar geometry or example a drift tube with a cylindrical cathode is approximated by a polygonal tube with several sides. Nevertheless, there are limitations and odd shaped electrodes occurring more frequently in novel gaseous detectors, which are not permitted, and neither are dielectric materials. This is made possible by using commercial packages like MAFIA [2] or MAXWELL [3], which deal with all sorts of geometry and materials. The extensively developed gas transport parameters simulation, MAGBOLTZ [4], has been integrated into GARFIELD, and interfaced with HEED [5], a program specifically developed for energy loss of charged particles, cluster characteristics, range and straggling of delta electrons, and photoionization. Thus, a complete simulation of charge transfer, drift, diffusion and multiplication of electrons in the detector and subsequent signal generation, including a positive ion movement, can be performed.

In this paper we will try to show how to compute the electrostatic fields in a three-dimensional model for a micro-pattern detector, the GEM, in MAXWELL, then import the field into GARFIELD, and subsequently, generate electrons and follow their paths, while they drift, diffuse and multiply in the electric field [6]. In a GEM, taken as an example, among other characteristics, it is important to know the electron transfer efficiency of the foil. The tools developed in conjunction with the aforesaid programs have been quite useful in computing and comparing with experiment, thus lending reliability to the predictive power for other applications.

Since the invention of the Micro-Strip Gas detector, over the last decade, a variety of micro-pattern detectors [7] have invaded the scene of charged particle tracking in a hostile high luminosity environment, replacing the traditional multiwire chambers with their higher rate capability. Made with simple printed circuit board technology, with through holes etched on double-sided metallized Kapton foils, typically 50 μm thick, the GEM [8] has been demonstrated to be a robust charged particle detector. Two foils in cascade form a Double GEM [9-11], delimited by a drift electrode above the first foil, and a signal collection electrode below the second. Due to its design, positive ion feedback into the drift region is reduced, when compared to that of a wire chamber [12].

Here, the electron drift properties are investigated and transparency has been computed and compared to experimental results; gain and positive ion feedback are also estimated.

2. Description of the Problem

Ansoft's 3D-Field Simulator (3DFS) is an electromagnetic Finite Element Method (FEM) solver [3]. It allows designers to experiment with various three-dimensional geometry, materials, and excitation levels (voltages). The program can be used to solve electrostatic, magnetostatic, and AC magnetic problems. The electric fields and potential gradients are solved for complex systems of conductors, charges and dielectrics. The software includes a solid modeller that allows a three-dimensional representation of the device or structure to be analysed. Once drawn, the materials and boundary conditions can be specified. A finite element mesh is analysed, eventually refined by the system/user, and the problem solved yielding fields and potentials in the whole volume.

---

[1] Address for correspondence: CERN, CH 1211, Geneva, Switzerland; e-mail Archana.Sharma@cern.ch

The GEM amplifies electrons released in a gas by ionising radiation. With appropriate potentials on the drift electrodes and across the GEM, and a grounded collection electrode, electrons enter the drift volume and are multiplied in the high electric fields in the GEM channels (E_H). The resulting avalanche of electrons provides sufficient gain for charged particle detection. To better understand their performance, simulation studies were started with 2D-models [13]. These were limited by the fact that the behaviour of the fields and potentials in regions between three adjacent holes could not be predicted or estimated, thus giving only a qualitative picture of the drift and multiplication properties of GEM. The geometry used throughout this work is as follows unless stated otherwise: 70 μm metal hole diameter, 50 μm Kapton diameter, and 140 μm pitch with staggered rows.

The question now is how to describe the GEM geometry in the 3DFS, so that the computed electric field has sufficient accuracy and can be used to predict an electron's path, as well as the avalanche multiplication mechanism in the real structure. The GEM structure modelled in this problem is shown in Fig. 1. The structure consists of a double-sided metallized Kapton dielectric, where holes have been etched, using a staggered array to maximise the channel density and optical transparency. Full transparency – or transmission of all electrons such that none are trapped on the top (or bottom) metallic surface – is one of the key design issues of the GEM. The inherent periodicity and symmetry of the structure should be exploited while making the model. There are several options while choosing the basic repetitive cell (see Fig. 2).
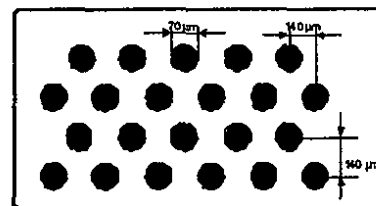

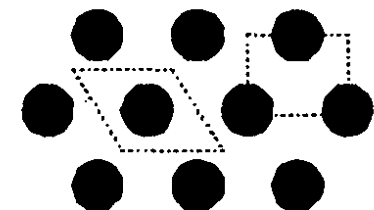Fig 1. Basic GEM structure.   Fig 2. Possible GEM basic cell definition.

One of the most important parts of the design with the 3DFS is the use of the CAD program for the structure description. This stage is time-consuming for the designer, as the complexity of these 3D-objects is high. Also, changing any given dimension often means a tedious and long redesign process.

In order to avoid these problems, a new methodology was explored in this project. It comprised of using the new scripting language from Ansoft to create a valid 3D-model automatically. The main advantage of this approach is that, once the script is programmed, any change can be easily inserted and the full model automatically recreated. A sample script for creating a basic GEM model is shown in Appendix 1. The new scripting language was studied and a first valid model was produced [15]. Thus, changing some of the dimensions became a trivial task and structural optimisations could be performed. The modelled 3D-structure of GEM is presented in Fig. 3.

Once the basic cell is chosen, the model should be drawn in the 3D-modeller and solved.

3. Problem Solution in the 3D-Field Simulator

Both basic repetitive cells were examined in the 3DFS. The first one, shown in Fig. 2, uses the basic hole with the 60 degrees lines. The materials were defined and the boundary conditions declared. However, there is a problem with the boundary conditions in this case, due to the dual-periodic nature of the structure. This led the simulator to compute the fields rather inaccurately, and the ensuing solutions were invalid. The second basic cell, also shown in Fig. 2, describes the problem differently. The four planes are parallel in this case, and thus the normal component of the electric field will always be null. With this knowledge, symmetry planes can be easily declared in the boundary manager and the solution can be computed accurately.
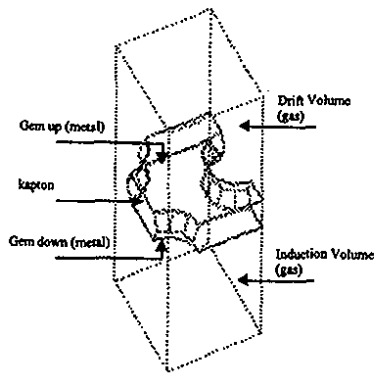
Fig. 3. GEM 3D-model: materials and volume description.

Fig. 4. Boundary Definitions.

3.1 Setting the Materials and Boundaries

In order to specify the problem, the materials must be assigned. The properties of the dielectric (permitivity and conductivity) of the metals allow the software to compute the electric fields. There are several predefined materials which can be assigned to the solids in a model defined in Maxwell; see Table 1. In addition, one can even define a new material given the permittivity and conductivity. Once this is done, the boundary assignment takes place. This includes the assignment of voltages to both metal planes, as well as the drift and ground potentials. In addition to these potentials, the four symmetric faces should be properly specified here, in order to model the infinite "sea of holes" GEM structure. Figure 4 shows this boundary assignment.

Fig. 5. Initial mesh.

Fig. 6. Manually refined mesh.

3.2 Manually refining the 3D-mesh

One of the problems while solving the model is that the automatically generated mesh is not properly defined in some of the regions where a good field solution is needed, i.e. close to the metal surfaces of the GEM hole. This can be tackled by manually refining the mesh in some volumes in the structure, as follows. Additional dummy objects are included in the definition of the structure. These dummy objects help to refine the initial mesh and increase the solution accuracy. Figure 5 shows the initial mesh, while Fig. 6 shows a manually refined mesh.

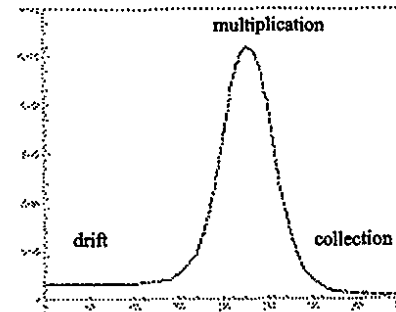Now the model is ready to be solved.

Fig 7. Electric field (V/m) through the GEM hole.

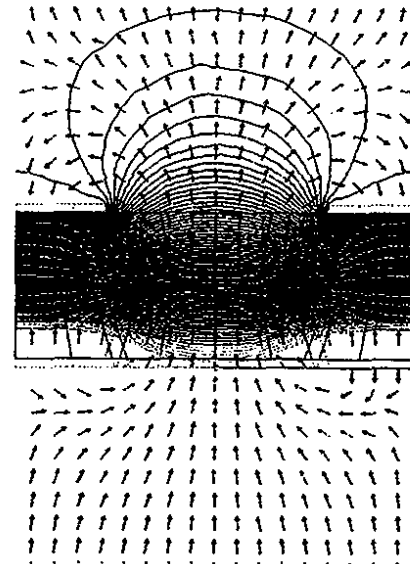

Fig. 8. The distribution of the equipotential lines and a vector plot of the electric field in a given plane that cuts the centre of the basic hole.

3.3 Solutions to the Problem

Figure 7 shows the magnitude of the electric field in a line running across the centre of the GEM hole, showing that high values present in this area will create the electron acceleration and multiplication – resulting in an avalanche effect. Figure 8 shows the distribution of the equipotential lines and a vector plot of the electric field in a given plane that cuts the centre of the basic hole.

4. Importing the field into GARFIELD

Once solved, the output from the MAXWELL may be written out and read into GARFIELD [9] in several files which describe the potentials, electric fields, and the materials of the problem at every node of the mesh of the numerous tetrahedral. Appendix II shows an example file, performing the following tasks:

- Read the electric field, voltages, and materials,
- Introduce the desired gas mixture,
- Plot field vectors in a given area or surface,
- Plot drift lines,
- Follow each electron with drift and diffusion and compute the end-points, and
- Introduce multiplication and follow the paths of electrons and ions until their end-points.

The field computed by using the 3D-model differs from that of the 2D, as exemplified in Figure 9 This is due to the metallic surfaces present both on top and the bottom of the GEM unaccounted for in the 2D-model, as well as the double conical Kapton well on either side. Figure 10 shows drift of electrons created by a track; one can appreciate the 3D-nature of the problem, observing that some of them go into neighboring staggered holes.
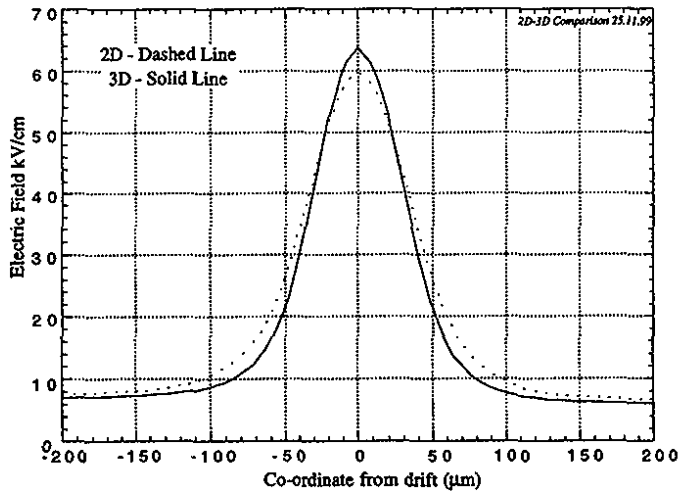

Fig. 9. The field computed using the 3D-model differs from that of the 2D-calculation.

4.1 Transparency of the GEM

More than on individual fields, the electrical transparency of the GEM depends on the ratio of drift to the dipole field (E_D/E_H), and its optical transparency [8]; a staggered matrix increases transparency as compared to straight rows of holes. Within the 3D-model, transparency has been computed generating uniformly a matrix of 2500 electrons on the drift electrode surface and following their path as they drift and diffuse down the channel[2]. Figure 11 shows the computed versus measured transparency for a single GEM.

[2] The Monte Carlo version of electron drift was used in Garfield.

The experimental values fall between those computed for holes with 70 µm and 80 µm diameter. This could well be the tolerance of the manufacturing process. Calculations for transparency in a nonzero magnetic field will be presented in section 4.
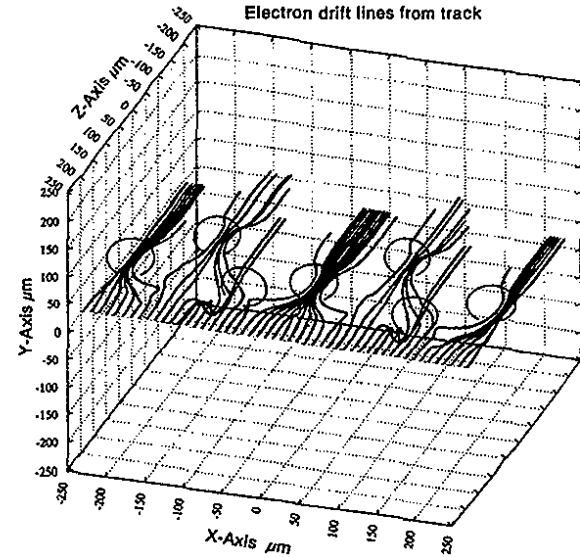

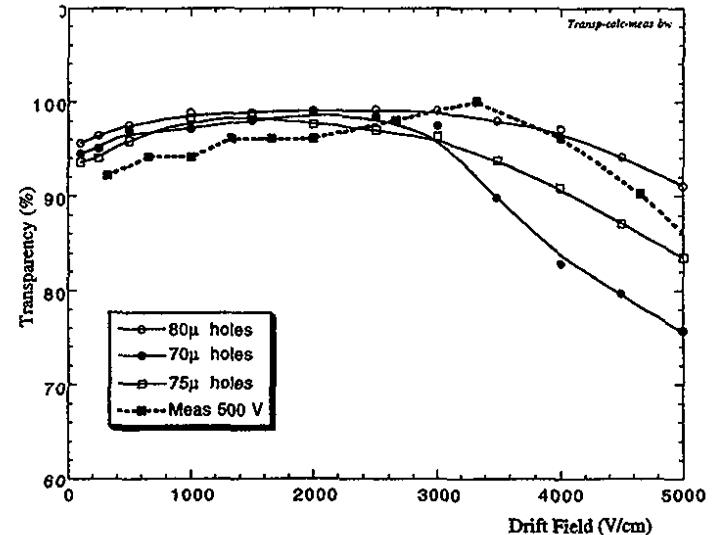Fig. 10. The plot shows drift of electrons created by a track.

Fig. 11. Computed versus measured transparency for a single GEM.

4.2 Avalanche, Effective Gain, and Positive Ions

The previous sections described how electrons move from the drift region into the GEM channels, and accounted for the loss of the electrons simply due to drift and diffusion. When electrons encounter the high field in the holes, they experience ionizing collisions thereby resulting in an avalanche of electrons, whose size depends on the dipole field. Some of the electrons of the avalanche are lost to the bottom electrode of the GEM, as seen in Fig. 12, consequently the 'effective' or visible gain of the multiplier is lower than the total number of ionizing collisions affected by a single electron [5]. The reliability of computations in this respect is quite low, since the Townsend coefficient is not very well known at high fields [10]; gains obtained from calculations differ up to factors of two to three when increasing the GEM voltage, as shown in Fig. 13. Detailed understanding of this discrepancy is being studied. The majority of the electrons are produced in the center; a doughnut of electron production is seen at the lower metal edge, Fig. 14, where the electric field is higher. This is a totally local effect; diffusion completely overtakes the field structure in GEM and ~ 200 μm below the GEM surface there is no trace of this effect; thus obliterating the GEM structure for any localization measurements.

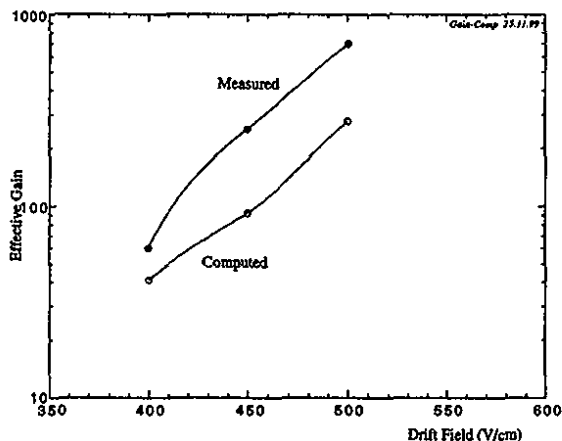Fig. 12. Some of the electrons of the avalanche are lost to the bottom electrode of the GEM.

Fig. 13. Gas gains obtained from calculations that differ up to a factor of two/three when increasing the GEM voltage.
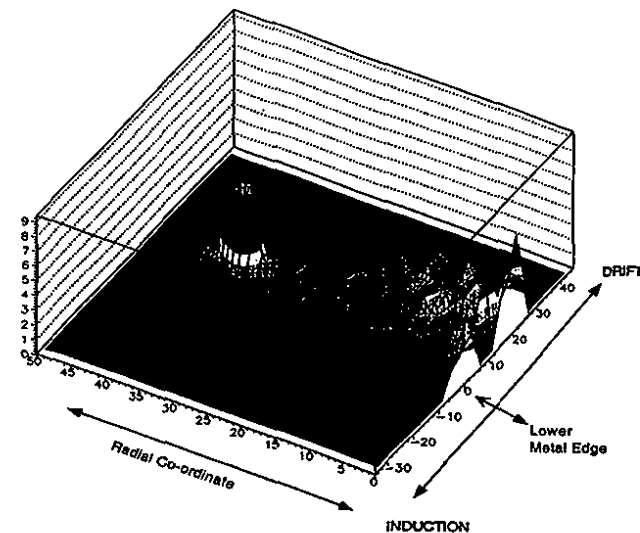

Fig. 14. The majority of the electrons are produced in the center.
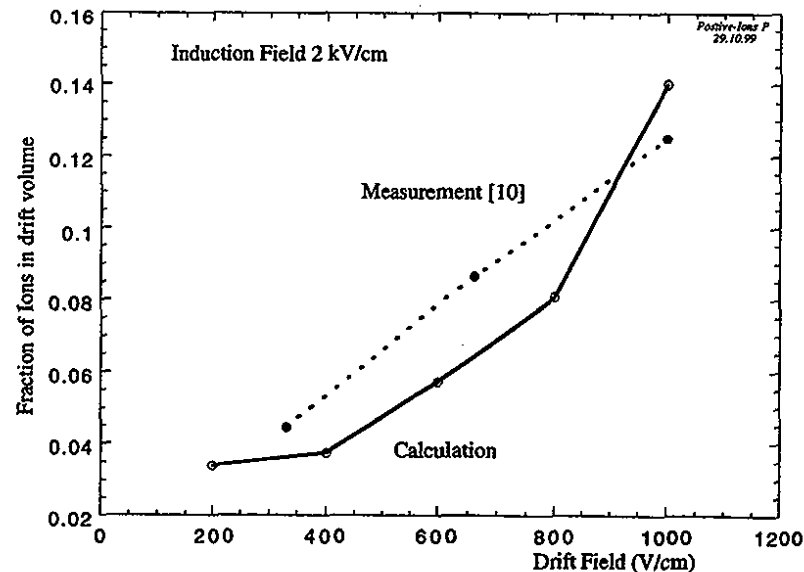

Fig. 15. The fractional number of positive ion feedback was also verified for a couple of voltage setting points at low drift fields. In general, the agreement with Ref. 8 is within 20%.

This results in making the mechanical alignment between two foils (Double GEM) redundant. Positive ions are produced essentially in the whole channel, but mostly in the vicinity of the lower GEM electrode; and move to the drift volume, the fraction depending strongly on the drift field [10]. It should be noted however, that the signal detected on readout (strips/pads) is totally due to the electron collection. There is no slow component due to the positive ion movement as compared to a traditional MWPC sense wire signal. The time taken by the positive ions to reach the GEM top typically corresponds to a few μs and few tens of μs to reach the drift electrode. The fractional number of positive ion feedback was also verified for a couple of voltage settings points at low drift fields, in general the agreement with [8] is within 20%, as shown in Fig. 15.

4. Operation of GEM in a high Magnetic Field

The qualitative behavior of performance in the presence of a strong electric field, perpendicular to the drift field, was investigated with the 2D-model [10], see Fig. 16. Despite several drift lines ending on the bottom of the foil, the lateral spread of the avalanche is enough to compensate for the loss of electrons due to the Lorentz force. Figure 17 shows the computed transparency and gain as a function of magnetic field (perpendicular to the electric field) with an Ar-CO$_2$ (70-30) gas mixture, and the electric field values as shown in the inset. One can see that while transparency drops dramatically (note that for these computations, a low drift field was chosen); there is no perceivable effect on the gain; measurements reporting no efficiency drop in the presence of a magnetic field have been published earlier [4]. The gas mixture as well as field configuration is by no means optimized; however, more work is needed in this direction.
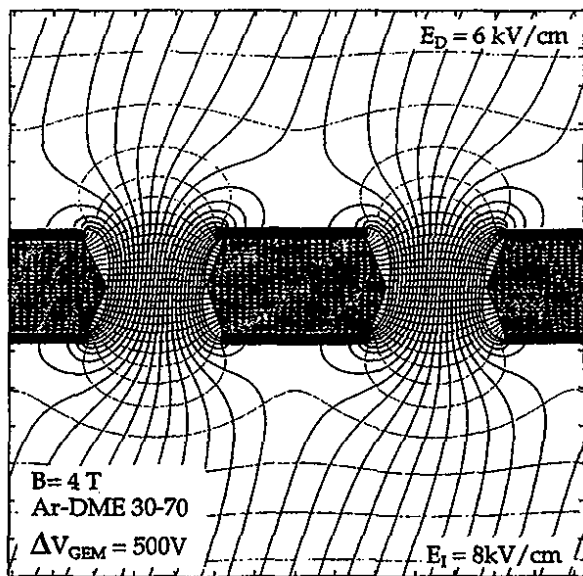

Fig. 16. The qualitative behavior of performance in the presence of a strong electric field perpendicular to the drift field was investigated with the 2D-model [10].
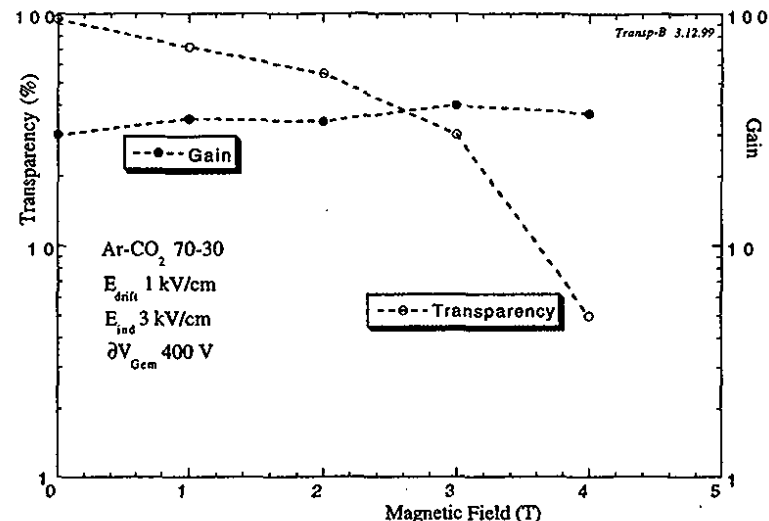

Fig. 17. The computed transparency and gain as a function of magnetic field (perpendicular to the electric field) with an Ar-CO$_2$ (70-30) gas mixture, and the electric field values as shown in the inset.

5. Conclusions

In this work, a three-dimensional simulation of the operation of a Gas Electron Multiplier has been performed describing the procedures in all detail. The results on transparency, positive ion feedback, and operation in magnetic field have been corroborated by experiment to within experimental errors. Comprehensive procedures for performing the simulation have been appended.

References
[1] GARFIELD, CERN Wire Chamber Field & Transport Computation Program written by R. Veenhof, Version 6.33.
[2] MAFIA, Commercial 3D-FEM electrostatic Solver, Darmstadt, Germany.
[3] MAXWELL Commercial Finite Element Computation Package, Ansoft Co., Pittsburgh, PA.
[4] S. Biagi, NIM A283(1989)716.
[5] I. Smirnov, HEED Simulation program for energy loss, St. Petersburg, integrated into GARFIELD by R. Veenhof.
[6] A. Sharma, Submitted to the Proceedings of Symposium on Application of Particle Detectors in Medicine, Biology, and Astrophysics, Seigen, Germany, 6-8 October 1999, also CERN OPEN 373/99.
[7] F. Sauli and A. Sharma, submitted for publication in Annual Rev. Sci. May 199, also CERN-EP/99-146.
[8] F. Sauli, Nucl. Instr. and Meth. A386 (1997) 531.
[9] J. Benlloch et al, IEEE Trans. Nucl. Sci. NS-45 (1998)531.
[10] C. Büttner et al, Nucl. Instr. And Meth. A409(1998)79.
[11] J. Benlloch et al, Nucl. Instr. And Meth. A419(1998)410.
[13] S. Bachmann et al CERN-EP/99-48, Submitted Nucl. Instr. And Meth. (1999).
[12] F. Sauli, Internal Report, CERN-EP-TA1, GEM Readout of the Time Projection Chamber Report (1999).
[14] F. Sauli and A. Sharma, Nucl. Instr. And Meth. A 323(1992)280-283.
[15] T. Motos-Lopez and A. Sharma, CERN Internal Report, CERN IT/99-05.

Table 1

Material	Relative Permittivity ----	Conductivity (μ) (siemens/meter)
Al₂O₃ Ceramic	9.8	0
Aluminum Nitride	8.8	2.2e06
Alnico 5	1	2e06
Alnico 9	1	0
Beryllium Oxide	6.8	0.0001
Ceramic 5	1	0
FR4	4.4	6.3e05
Nd Fe 30	1	0
Teflon	2.2	0
Air	1.0006	0
Alumina	9.4	3.8e07
Aluminium	1	1e-09
Bakelite	4.8	0
Benzocyclobuten	2.6	0
Beryllium	1	1.5e07
Brass	1	1e07
Cast Iron	1	1.5e06
Chromium	1	7.6e06
Cobalt	1	1e07
Copper	1	5.8e07
Corning Glass	5.75	0
Cyanate Ester	3.8	0
Diamond	16.5	1e-13
Diamond Hi Pressure	5.7	0
Diamond CVD	3.5	0
Duroid	2.2	0
Epoxy-Kevlar	3.6	0
Ferrite	12	0.01
Gallium Arsenide	12.9	0
Glass	5.5	1e-12
Glass-PTFE	2.5	0
Gold	1	4.1e7
Graphite	1	7e04
Iron	1	1.03e07
Kapton	3.3-5.5	0
Lead	1	5e06
Marble	8.3	1e-08
Mica	6	1e-15
Mu-Metal	1	1.61e06
Nickel	1	1.45e07
Palladium	1	9.3e06
Perfect-Conductor	1	Infinity
Platinum	1	9.3e06
Plexiglass	3.4	0.0051
Polyamide	4.3	0

Polyethylene	2.25	0
Polyamide-Quartz	4	0
Polystyrene	2.6	1e-16
Porcelain	5.7	1e-14
Quartz-Glass	3.78	0
Rubber-Hard	3	1e-15
Sapphire	10	0
Silicon	11.9	0
Silicon Dioxide	4	0
Silicon Nitrate	7	0
Silver	1	6.1e07
Soldeer	1	7e06
Stainless Steel	1	2e06
Tantalum	1	6.3e06
Teflon	2.8	0
Titanium	2.8	0
Tungsten	1	1.82e07
Vacuum	1	0
Water	81	0.0002
Zinc	1	4

Appendix I

```
# This script will create the geometry for the gem3D problem, with the
# basic cylindrical hole structure.
#
# First, let's declare the important variables.
# Note that all dimensions are in microns.
# THIS IS WHERE YOU SHOULD CHANGE THE NUMBERS !!

clearall
setunits "microns" "y"

assign side 140
assign int_diam 50
assign kapton_h 50
assign copper_h 5
assign up_size 250
assign down_size 250


# YOU SHOULD NOT NEED TO CHANGE ANYTHING BELOW THIS
# Let's do some calculations for the useful numbers...

assign xmax div side 2
assign xmin mul xmax -1          # Minimum x
assign ymax div side 2
assign ymin mul ymax -1          # Minimum y

assign int_rad div int_diam 2    # Compute internal radius

assign zmed div kapton_h 2       # The kapton is centered in z axis
assign n_zmed mul zmed -1        # the negative value
assign lower sub n_zmed copper_h   # the first copper below
assign zmin sub lower down_size    # and the minimum dimension now
assign upper add zmed copper_h     # Now the symmetrical, up.
assign zmax add upper up_size

assign total_h add kapton_h (mul copper_h 2)   # kapton + 2 coppers

# STEP 0. Clear everything.

if GT getnumobjects 1
  delete "*"
end

# STEP 1.
#
# Let's draw the initial box that will be later divided into the copper and
# kapton.

box pos3 xmin ymin lower side side total_h "brick"
Recolor "brick" 255 0 0

# STEP 2
#
```

```
# Now we are going to draw the hole in the brick.

cyl pos3 0 0 lower 2 int_rad total_h "hole"

# STEP 3
#
# Now this object is substracted from our initial brick.

subtract "brick" "hole"

# STEP 4
#
# Let's chop now the brick to create the upper and bottom copper.

origin pos3 0 0 n_zmed
split 2 2 "brick"
assign npiece getobjectname getnumobjects
rename npiece "down"

globalcs

origin pos3 0 0 zmed
split 2 2 "brick"
assign npiece getobjectname getnumobjects
rename npiece "kapton"

rename "brick" "up"

globalcs

recolor "up" 0 255 0
recolor "down" 0 255 0


# STEP 6. Finally, create the external boundary. In order to do this,two
# dummy objects will be created, above and below the main one. This can
# also help later with manual meshing.

box pos3 xmin ymin zmin side side down_size "dummy_down"
box pos3 xmin ymin upper side side up_size "dummy_up"

recolor "dummy_down" 0 128 128
recolor "dummy_up" 0 128 128
hide "dummy_down"
hide "dummy_up"

fitregion 0 "n"
recolor "background" 128 128 128
```

```
Global field True
Global drift True
Global trans True
Global gain True
Global esurf = 0
Global etran = 0
Global ekap  = 0
Global random True
Global mc False
&CELL
Global dir `~/Maxwell/3D/75mu.pjt`
Global bin `3D.bin`
Call inquire_file(bin,exist)
If exist Then
  read-field-map {bin}
Else
      field-map files "{dir}/v.reg" ...
      field-map files "{dir}/e.reg" ...
    field-map files "{dir}/d.reg" ...
          x-mirror-periodic y-mirror-periodic ...
          histogram-map
  save-field-map {bin}
Endif
&GAS
Ar-50-eth-50
If field Then
&FIELD
area -0.05 -0.05 0.05 0.05 view z=0
*pl vect
area -0.025 * -0.025 0.025 * 0.025 view y=0
*pl vect
*pl cont
area -0.020 -0.020 * 0.020 0.020 * view z=0.0050
grid 50
pl surf ez angles 60 120
Endif
If drift Then
&DRIFT
area -0.025 * -0.025 0.025 * 0.025 view x=0 rotate -90
track 0.0010 -0.025 0.020 0.0010 0.025 0.020 lines 50
int-par max-step 0.0001 int-acc 1e-11 nocheck-kink
dr tr
Endif
If trans Then
  &DRIFT
  int-par max-step 0.0005 int-acc 1e-11 noreject-kink m-c-dist-int 0.0002
  Global xmin=0
  Global xmax=sin(60*pi/180)*0.014
  Global ymin=-0.0070
  Global ymax=+0.0070
  Global z=0.0190
  Global n=25
```

```
*   area -0.025 -0.025 -0.0250 +0.0250 +0.0250 0.0250 view z={z}
    area -0.005 -0.02 -0.0250   +0.015 +0.02 0.0250 view z={z}
*   area view x+2*y+3*z=0 3d
*   tr -0.050 0.0 0.019 0.050 0 0.019 lines 50
*   dr tr
*   tr -0.050 0.007 0.019 0.050 0.007 0.019 lines 50
*   dr tr
    !rep function-1 polymarker-colour red marker-type circle marker-size 0.2
    !rep function-2 polymarker-colour blue  marker-type circle marker-size 0.2
    !rep function-3 polymarker-colour green   marker-type circle marker-size 0.2
    Call plot_drift_area
    For i From 1 Step 1 To n Do
      For j From 1 Step 1 To n Do
        If random Then
            Global x=xmin+(xmax-xmin)*rnd_uniform
            Global y=ymin+(ymax-ymin)*rnd_uniform
        Else
            Global x=xmin+(i-1)*(xmax-xmin)/(n-1)
            Global y=ymin+(j-1)*(ymax-ymin)/(n-1)
        Endif
        If mc Then
            Call drift_mc_electron(x,y,z,status)
        Else
            Call drift_electron_3(x,y,z,status)
        Endif
        Call plot_drift_line
        Call get_drift_line(xd,yd,zd,td)
        Call drift_information(`steps`,nd)
        If nd<1 Then Iterate
        Global zend=number(zd[nd])
        If zend>+0.0050 Then
          Say "Stopped, (x,y,z)=({x,y,z}), status={status}, zend={zend}"
          Call plot_marker(x,y,`function-1`)
          Global esurf=esurf+1
        Elseif zend<-0.0005 Then
*         Say "Through, (x,y,z)=({x,y,z}), status={status}, zend={zend}"
          Call plot_marker(x,y,`function-3`)
          Global etran=etran+1
        Else
*         Say "Kapton, (x,y,z)=({x,y,z}), status={status}, zend={zend}"
          Call plot_marker(x,y,`function-2`)
          Global ekap=ekap+1
        Endif
      Enddo
    Enddo
    Call plot_end
    Say "(esurf,ekap,etran)=({esurf,ekap,etran})"
Endif


&DRIFT
  area -0.025 -0.025 -0.0250   +0.025 +0.025 0.0250 view y=0 rot 180
  int-par max-step 0.0005 int-acc 1e-11 noreject-kink m-c-dist-int 0.0002
  Global plotdrift False
  If plotdrift Then
```

```
Global opt `plot-electron,plot-ion`
Else
   Global opt `noplot-electron,noplot-ion`
Endif
Call book_histogram(drift,100)
Call book_histogram(top,100)
Call book_histogram(kapton,100)
Call book_histogram(down,100)
Global tot=0
Global niter 100
For i From 1 To niter Do
   Say "Avalanche {i}/{niter}"
   If plotdrift Then Call plot_drift_area
   Call avalanche(0.001,0,0.020, opt, ne, ni, ...
      `t_ion, z_ion>0.0060`          ,drift, ...
      `t_ion, z_ion<0.0060&z_ion>0.0050` ,top, ...
      `t_ion, z_ion<0.0050&z_ion>0`      ,kapton, ...
      `t_ion, z_ion<0    &z_ion>-0.0010`,bottom, ...
      `t_ion, z_ion<-0.0010`          ,through)
   Global tot=tot+ni
   If plotdrift Then Call plot_end
Enddo
Call plot_histogram(drift,`Time [microsec]`,`Ions to drift region`)
Call plot_end
Call plot_histogram(top,`Time [microsec]`,`Ions to GEM top`)
Call plot_end
Call plot_histogram(kapton,`Time [microsec]`,`Ions to kapton`)
Call plot_end
Call plot_histogram(bottom,`Time [microsec]`,`Ions to GEM bottom`)
Call plot_end
Call plot_histogram(through,`Time [microsec]`,`Ions in collection`)
Call plot_end
Call inquire_histogram(drift, exists, set, channels, ...
   minimum, maximum, entries, average, sigma)
Say "To drift region: {entries}/{tot}"
Call inquire_histogram(top, exists, set, channels, ...
   minimum, maximum, entries, average, sigma)
Say "To GEM top:     {entries}/{tot}"
Call inquire_histogram(kapton, exists, set, channels, ...
   minimum, maximum, entries, average, sigma)
Say "To kapton:      {entries}/{tot}"
Call inquire_histogram(bottom, exists, set, channels, ...
   minimum, maximum, entries, average, sigma)
Say "To GEM bottom: {entries}/{tot}"
Call inquire_histogram(through, exists, set, channels, ...
   minimum, maximum, entries, average, sigma)
Say "To collection: {entries}/{tot}"4
Endif
```

DETECTION OF PHOTONS IN THE HERA-B RICH

P. Križan

J. Stefan Institute and University of Ljubljana, Slovenia

for the HERA-B RICH Group*

ABSTRACT

The tests carried out with the photon detector of the ring imaging Cherenkov detector for the HERA-B experiment are reviewed. Results of on-the-bench tests of the employed photomultiplier tubes are reported together with early commissioning measurements with the HERA proton beam.

---

1 Introduction

The HERA-B experiment [1] aims at measuring: CP violation in $B^0 \to J/\psi K_S^0$ and $B^0 \to \pi^+\pi^-$ decays, $B_s^0 \bar{B}_s^0$ mixing and $B\bar{B}$ decays with two leptons in the final state. The B mesons will be produced in collisions of 920 GeV/c protons with a fixed target. The target consists of eight wires in the halo of the proton beam in order not to disturb experiments measuring ep collisions.

One of the essential components of the spectrometer is the ring imaging counter (RICH), with the prime function of separating kaons from pions [1-4]. In what follows, we shall briefly describe the essential components of the RICH counter, and will then discuss in detail the detection of photons.

2 The HERA-B RICH

The main purpose of the ring imaging Čerenkov counter in the HERA-B experiment is the tagging of the B meson flavor. Tagging of the B^0, or the $\overline{B^0}$ meson, is accomplished by identifying the charged

*The HERA-B RICH Group is a collaboration of the University of Texas at Austin, University of Barcelona, LIP Coimbra, Northwestern University, Evanston, DESY Hamburg, University of Houston, J. Stefan Institute, Ljubljana, and University of Ljubljana.

kaon into which the associated B meson decayed. The momentum distribution of charged kaons, resulting from decays of the B mesons, is shown in Fig. 1. Identifying the charged kaon essentially
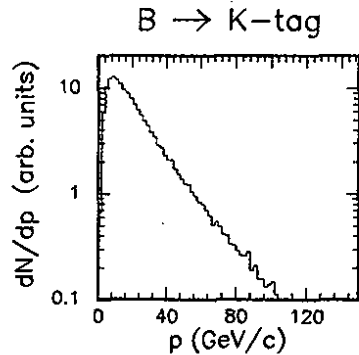
$$B \rightarrow K-tag$$

Figure 1: The momentum distribution of charged kaons produced in decays of B mesons associated to the production of a B^0 or $\overline{B^0}$ meson by proton nucleus interactions at HERA-B.

means separating it from the pion of the same momentum. Since the momentum is accurately measured in other components of the HERA-B detector, the separation in mass is equivalent to the separation in velocity, for which the RICH counter is employed.

Perfluorobutane gas (C_4F_{10}) has been chosen for the HERA-B RICH radiator, since it combines a relatively high-refractive index and a low dispersion. In this gas, the Čerenkov radiation threshold momenta for pions and kaons are at 2.7 GeV/c and 9.6 GeV/c, respectively. For $\beta = 1$ particles, the Čerenkov angle is 51.5 mrad, while the $\pi - K$ difference in Čerenkov angle is 6 mrad at 20 GeV/c and falls to 0.9 mrad at 50 GeV/c.

The set-up of the counter is schematically shown in Fig. 2. The two spherical mirror halves are tilted, i.e., the center of curvature of each half mirror is displaced relative to the target position, by which photons are reflected to photon detectors well outside the charged particle flux.

The 108 m^3 vessel for the C_4F_{10} gas radiator has been constructed from stainless steel, except for the particle entry and exit windows (1 mm Al), and the photon exit windows (UVT perspex). Also, two-beam shrouds close the gas volume around the two beam pipes for protons and electrons are constructed. The purification and circulation system for the C_4F_{10} gas has been constructed at CERN and was commissioned at DESY. It is worth noting that the initial filling of the volume amounts to about 1100 kg of C_4F_{10}.

Two mirror systems, a spherical and a planar one, are made of hexagonal and rectangular units, respectively. The hexagonal mirror segments with 11.4 m radius of curvature have been produced
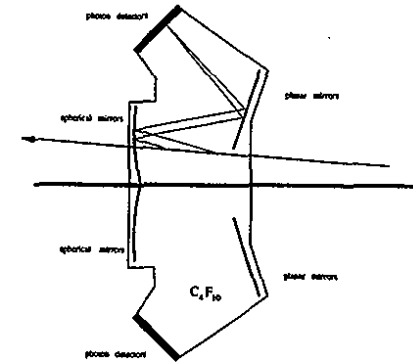

Figure 2: The HERA-B RICH.

of 7 mm thick grinded glass. The mirror quality has been determined upon delivery by measuring the radius of curvature for each segment, and the fraction of reflected light, as well as by recording a Ronchi image to check the homogeneity of the mirror surface. The reflectivity was required to exceed 85% in the wavelength interval of 250 - 600 nm. Each spherical mirror segment is supported at three points, two of which can be moved, and are motor driven via a transmission mechanism with a feed through to the exterior of the vessel. The planar mirrors are made of float glass, thus being significantly cheaper at the required optical quality. By making use of the data gathered on all the mirror segments, it was possible to group them in the tiling scheme according to their optical quality and resolution requirements [5].

3 Photon Detector

Initially, two wire chamber based photon detectors were considered, a CsI photocathode in a MWPC and a TMAE-based detector with 10 cm deep, and 8 x 8 mm^2 unit cells. After the considerable success of on-the-bench and beam tests [6-8], the detectors were tested in a high-rate environment as expected in the HERA-B experiment. Both wire chamber-based detectors had to be abandoned; the TMAE detector showed a prohibitive decrease of avalanche gain due to aging effects [9,10], while the CsI photocathode could not be routinely produced and maintained with sufficiently high quantum efficiency, in addition to problems with rates in excess of a few kHz per pixel [11,12].

The final photon detector considered was the Hamamatsu multianode R5900 M16 and M4 photomultiplier tubes, which became available just at the time when it was realised that an alternative solution is needed. The M16 version has 16 pads of 4.5 x 4.5 mm^2 each, with a 12-stage, metal-foil
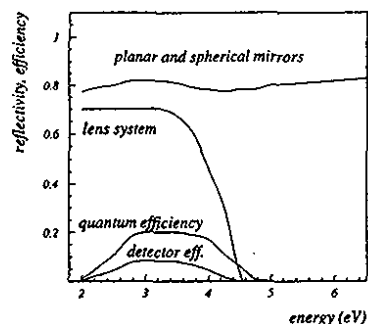
Figure 3: *Reflectivity of planar and spherical mirrors and the detection efficiency of the photon detector as a function of photon energy. The photon detector efficiency is a product of the photomultiplier tube quantum efficiency, the photoelectron detection efficiency and the transparency of the optical system.*

dynode system [13]. The M4 version has four pads of 9 x 9 mm^2 each and ten dynodes. The quantum efficiency of the photocathode with a borosilicate window has a broad plateau in the wavelength region between 300 nm and 500 nm with a maximum value of 20% (Fig. 3). The UV-extended version has a UV transparent window, which shifts the low wavelength cut-off to about 250 nm. The other PMT characteristics such as the required cathode high voltage ($\leq$ 1000 V), the current amplification (10^7), dark current ($\sim$ 1 nA), pulse rise time (0.8 ns), transit time spread (0.3 ns) [13], are also satisfactory.

The outer dimensions of the PMT are 28 x 28 mm^2, so the photocathode occupies only about 30% of the surface. Due to the smaller photocathode surface compared to the photomultiplier cross section, a two lens demagnification system (2:1) was designed (Fig. 4) [14]. The lenses are made of UVT perspex with high transparency over most of the wavelength region, where the photocathode is sensitive (Fig. 3). The angular acceptance of the optical system is also satisfactory and is uniform for incident angles below about 110 mrad [15]. In addition to increasing the active area, the lens system also adjusts the required pixel size in the central detector region (9 x 9 mm^2) to the PMT pad size 4.5 x 4.5 mm^2. The outer detector region with lower occupancy and looser resolution requirements, uses the M4 version of the tube with two times larger pads (9 x 9 mm^2) with the same lens system, such that the pixel size amounts to 18 x 18 mm^2.

The base board accepts four PMT's and provides positioning. In addition it houses the voltage divider, signal lines, and the front-end electronics consisting of 16-channel boards based on the
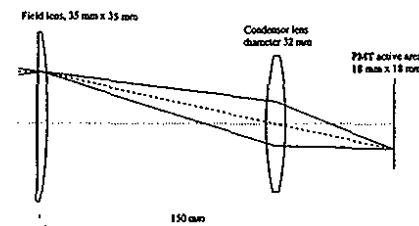
Figure 4: *The optical system for light collection and demagnification. The two rays shown in full line correspond to photons with incident angles of $\pm$100 mrad.*

ASD8 chip [16]. In Fig. 5, a photograph of a fully equipped basic module for the M16 photomultiplier tubes is presented.
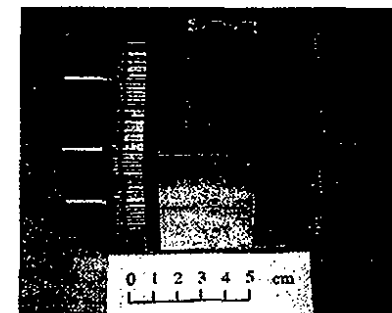

Figure 5: *Fully equipped photomultiplier basic module with the Hamamatsu R5900 photomultiplier tubes type M16.*

In order to reduce the contribution of spherical aberration to the overall resolution of the Čerenkov angle, an optimal surface of the Čerenkov photon detector has been calculated [17,18]. Each half-detector (upper and lower) consists of five flat supermodules placed in order to approximate the optimal surface, which is close to the shape of a flattened (ellipsoidal) cylinder. Such an arrangement also ensures better acceptance for the Čerenkov photons, which should be incident onto the flat supermodules at angles below 110 mrad.

From the data available on the quantum efficiency, mirror reflectivities, window and optical system transmissions (see Fig. 3), one calculates the merit factor $N_0 = 43$ cm^{-1}, such that the expected number of photons for particles approaching the velocity of light amounts to $N_{det} = N_0 L \sin^2 \vartheta = 31$ with $L = 2.7$ m and $\vartheta = 51.5$ mrad. The expected single photon resolution is 0.7 mrad and 1 mrad for the regions occupied by M16 and M4 PMT's, respectively.

4   Measurements and Results

4.1   Multianode PMT as a
Single Photon Counter

In the initial set of measurements [20] the single photon counting properties of the tube were investigated, in particular the efficiency for single photon detection as well as the background count rate. In this phase three multianode PMT's were tested; one with borosilicate glass window (serial no. 6A19C4) and two with UV transparent windows (serial no. 5M26C6 and serial no. 6C22C5). The tubes were of the 16-channel photomultiplier tube assembly type which includes a voltage divider circuit (Hamamatsu type H6568).

In the experimental set-up shown in Fig. 6 it was established that the tube allows for good single photoelectron detection as may be seen in Fig. 7. The average pulse height on each of the pads
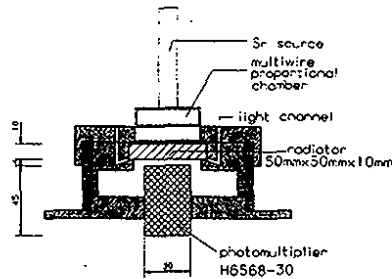
Figure 6: *The set-up for testing the PMT properties on the bench. Čerenkov photons, emitted by* ^{90}Sr β *particles in a solid radiator, are used as a stable light source [21].*

is shown in Fig. 8. These data were obtained by allowing a small leak of daylight into the crystal radiator from which the photon reached the photocathode more or less uniformly illuminating its surface.

The bleeder chain was optimized by varying the composition of the 13 resistors [22]. Very little dependence of rate at the high voltage plateau was seen when varying the fraction of the 1 MΩ to 560 kΩ resistors. Somewhat better results were obtained with the first three steps of 1 MΩ resistors, followed by ten 560 kΩ resistors. This bleeder chain was then adopted for the M16 photomultiplier tube. For the M4 photomultiplier a similar voltage divider was chosen, where again the first three resistors had twice the value of the other eight.
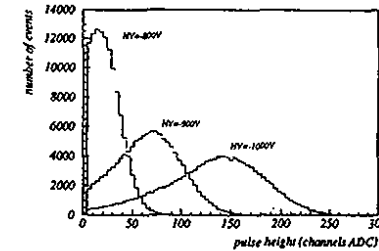
Figure 7: *The measured pulse height distributions of the M16 PMT due to single photoelectrons for different high voltage values.*

Cross talk has been estimated by observing simultaneous pulses on adjacent pads, when the pulse on one pad has been recorded to be above a certain threshold. The pulse height spectra, triggered by pad number 7 are shown in Fig. 9. The cross talk is estimated from this figure to be 0.2% between direct neighbors and only 0.1% between diagonal neighbors.

Ageing was studied [20] by illuminating the photocathode pads with a 5 W neon bulb through a small hole at one side of a 1 m long, 10 cm diameter black plastic tube with the PM on the other side. No reduction of the 3 MHz counting rate has been observed over a 30-day period of continuous illumination and operation.
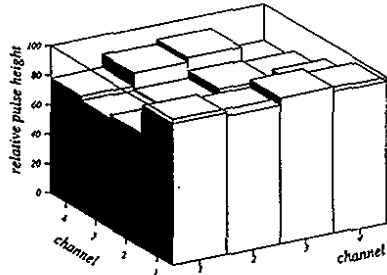
Figure 8: *Lego plot of the average single photoelectron pulse heights normalised to the pad with the largest average pulse height.*
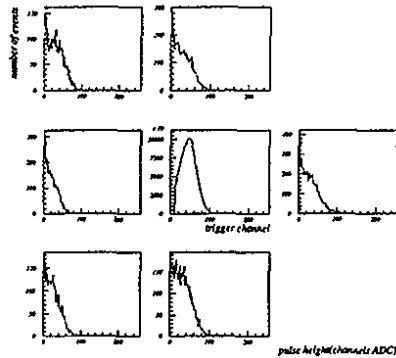

Figure 9: *Cross talk has been measured by triggering with one of the channels and observing simultaneous pulses on six neighbouring channels.*
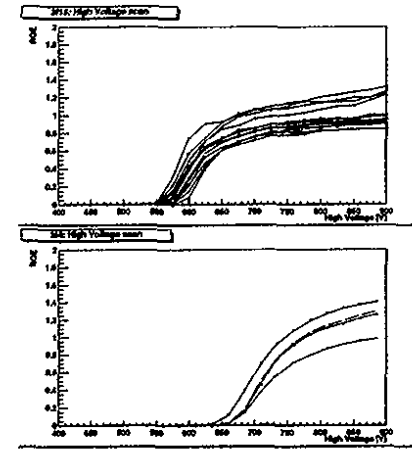
4.2 Results of Quality Assessment Tests

Figure 10: *Dependence of the suitably normalized rate (channel count rate divided by 1000 and 4000 for M16 and M4 PMT's, respectively) as a function of the high voltage for all channels of a representative M16 (above) and M4 (below) photomultiplier tube.*

Tests of all the 2305 PMT's (1543 M16's and 762 M4's) have been made in the laboratory prior to the installation in the photon detector [23]. The apparatus employed is similar to the one shown in Fig. 6. Again, Čerenkov photons produced by β electrons of the ^{90}Sr source were used as a stable light source. In this case four tubes were tested at the same time, of which one was used as a reference. For each photomultiplier tube, the source and background rates were recorded as a function of high voltage and threshold setting (Figs. 10-12). On the basis of these tests, the photomultipliers have been grouped according to similar high voltage characteristics, allowing all PMT's within a group to be connected to the same high voltage, thus maximising the efficiency for the given, much smaller number of independent HV channels [19]. The results obtained for the optimal high voltage, as well as for the relative PMT sensitivity, were compared to values provided by the manufacturer, and a good agreement was found [23].

Figure 13 gives the distribution of M4 and M16 photomultipliers versus their recommended high voltage value as obtained in the quality assessment tests. This value is seen to be larger for M4's than for M16's, which is a consequence of the smaller number of dynodes (10 for M4's compared to 12 for M16's). The distributions of photomultipliers depending on their normalized count rate (channel count rate divided by 1000 and 4000 for M16 and M4 PMT's, respectively) at
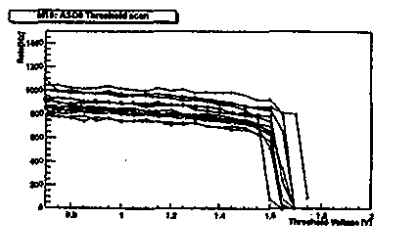
Figure 11: *Dependence of the count rate on the threshold voltage for a typical M16 photomultiplier tube.*

the recommended value of high voltage are shown in Fig.14 separately for M16's and for M4's.

Finally Fig.15 shows the time dependence of the rate per channel of the reference M4 and M16 photomultipliers in the quality assessment tests. The count rate decrease is consistent with the known decay rate of the ^{90}Sr source.

From the quality assessment tests relative surface sensitivity of each tube could be determined, after correcting for a slightly nonuniform illumination of the surface. An example for each of the PMT types is shown in Fig. 16.

To further investigate the variation of sensitivity over the photomultiplier surface, a scan was carried out for selected PMT's by using a light beam spot of about 20 μm diameter [24]. From Fig. 17 the pad and dynode channel structure can clearly be seen.
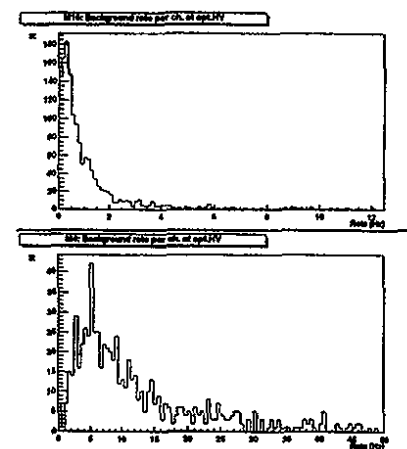
Figure 12: *Distribution of M16 (top) and M4 (bottom) channels depending on their background count rate.*
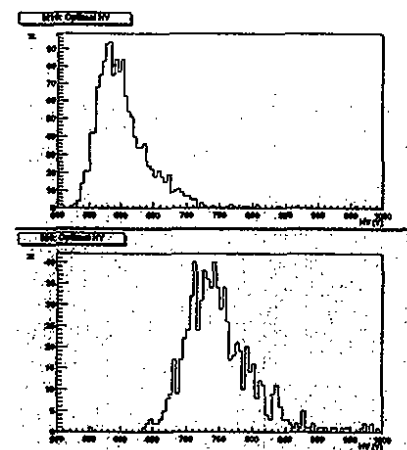
Figure 13: *Distribution of M16 (top) and M4 (bottom) photomultipliers depending on the value of their recommended high voltage.*
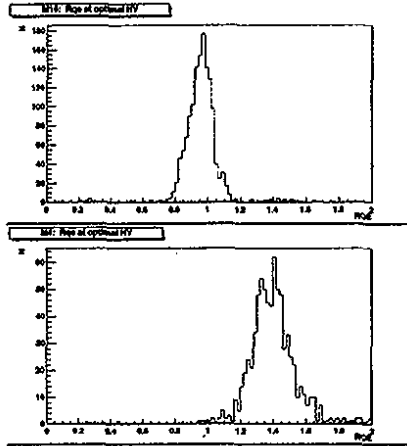
Figure 14: *Distribution of M16 (top) and M4 (bottom) photomultipliers according to their normalized count rate (RQE) at the recommended voltage.*

Figure 16: *Relative sensitivity of each pad of representative M16 and M4 photomultipliers as determined by illuminating the whole surface.*
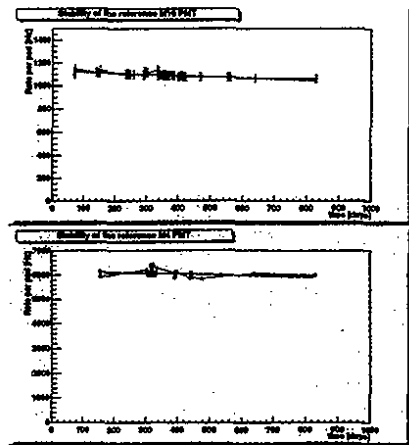

Figure 15: *The time dependence of the count rates of the reference photomultipliers; M16 (top diagram), M4 (below). The curves represent the radioactive decay of ^{90}Sr.*
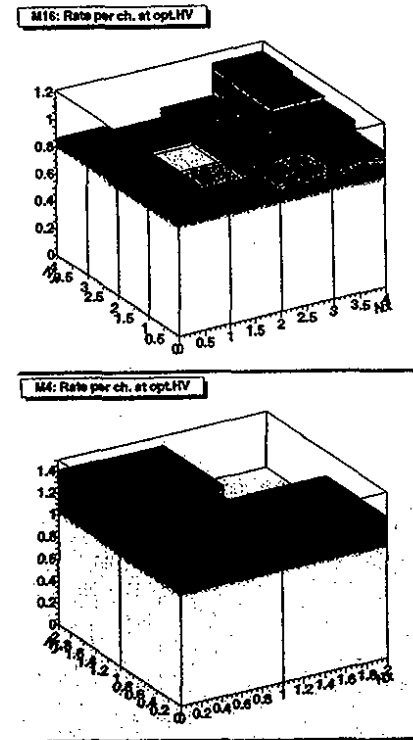
4.3 Test Measurements In Situ

With the photon detectors in their proper position in the HERA-B spectrometer, the photomultipliers cabled to the readout system and with freon as Čerenkov radiator, the commissioning of the system became possible. Fig. 18 gives the count rate versus high voltage for one of the M16 and one of the M4 photomultipliers. It is seen that the curves measured in situ with the HERA proton beam agree nicely with the ^{90}Sr source measurements. The occupancy is shown in Figure 19, where the region occupied by M16 PMT's is clearly distinguished from the region occupied by M4 PMT's. We also note that only about 0.3% of the nearly 30,000 channels were found to be noisy, and were excluded from further analysis.
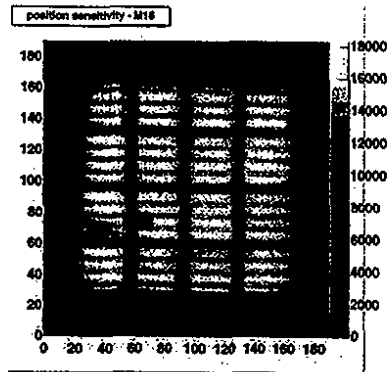

Figure 17: *Sensitivity of a M16 PMT surface when scanned by a light beam spot of about 20 μm diameter.*
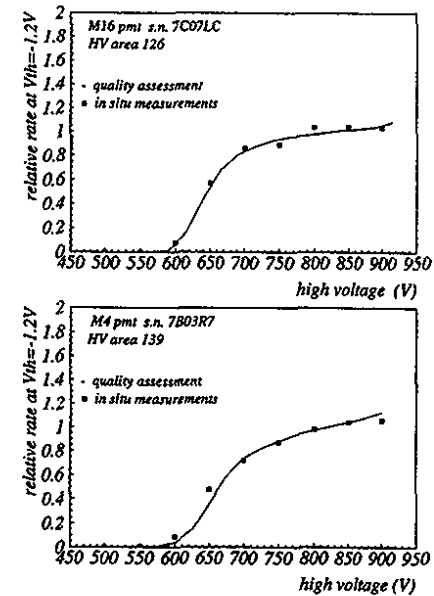

Figure 18: *The plateau curves for a M16 (top) and a M4 (bottom) photomultiplier tube. The data labelled 'in situ' represent values measured during the photon detector testing in its final position, while the curves labelled "quality assessment" correspond to measurements made in the laboratory during on-the-bench quality tests. The data are normalised to the average of the three points at 750 V, 800 V, and 850 V.*

The performance of the RICH detector was also checked by varying the interaction rate of the wire target. In a set of measurements, the response of the detector was recorded at target rates
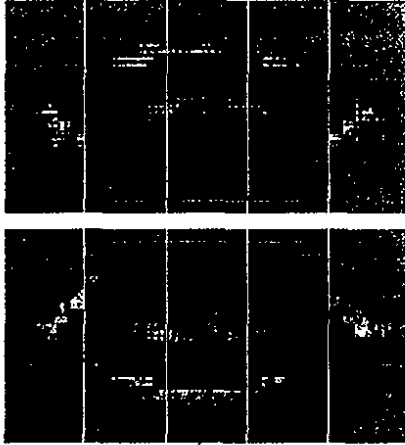
Figure 19: *The occupancy of the upper and lower photon detectors shows the region occupied by M16 (inner region) and M4 PMT's (outer region).*

from 1 MHz up to the design value of 40 MHz. In Fig. 20, the accumulated number of hits on the photon detector as a function of target interaction rate is presented, and a good linearity can be seen.

Due to the nonavailability of the information from the particle tracking system, the Čerenkov ring radii were deduced by finding the rings which best fit the detected hits on the photon detector. Only events which depict well-separated Čerenkov rings were employed in a simple analysis [25]. In the analysis, one counts the detected photons per Čerenkov ring by looking at appropriate events (two of which are shown in Figs. 21 and 22) and measures the corresponding ring radius. The number of counted hits per Čerenkov ring is plotted as a function of the measured Čerenkov angle in Fig. 23. The lines drawn on the plot correspond to a hypothesis that $31 \pm \sqrt{31}$ photons are radiated from particles approaching the velocity of light.

For each of the rings recorded in Fig. 23, we calculated the photon detector response parameter N_0. The resulting distribution is shown in Fig. 24. We observe that the average value of the photon detector response parameter, as well as the average number of detected photons per ring, are consistent with expectations.
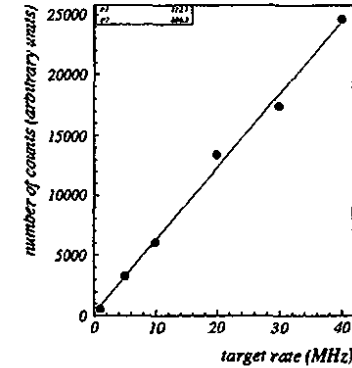

Figure 20: *Accumulated number of hits on the photon detector versus target interaction rate. Noisy channels (in total about 0.3%) are suppressed.*
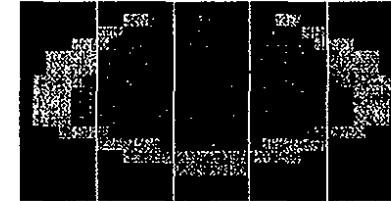

Figure 21: *Display of an event on the lower photon detector with a single Čerenkov ring consisting of 33 detected photons. From the ring radius Čerenkov angle of 51.9 $\pm$ 0.5 mrad is deduced for which 31 $\pm$ 2 detected photons would be expected.*

5 Summary

A detector of Čerenkov photons for a high-rate environment of the HERA-B experiment was designed, tested, installed, and commissioned. A preliminary data analysis shows that the design goals, a figure of merit $N_0 = 43$ cm^{-1}, resulting in 31 detected photons on a saturated Čerenkov ring, was met. We also note that the resolution as determined from a stand-alone ring search analysis [26] is consistent with the design values of 0.7 mrad and 1 mrad for M16 and M4 tubes, respectively.
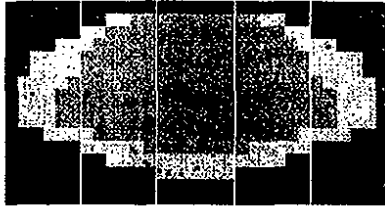
Figure 22: *Two intersecting Čerenkov rings, one with 22 photons detected by four and sixteen channel photomultiplier tubes, a measured Čerenkov angle of 45.5 ± 0.5 mrad and expected number of 23.8 ± 1.5 hits, and a ring with 27 photons detected exclusively by sixteen channel photomultiplier tubes, 49.8 ± 0.5 mrad Čerenkov angle and expected 28.5 ± 1.8 hits.*
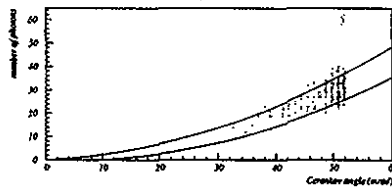

Figure 23: *Measured (data points) and expected (±σ curves) number of detected photons versus Čerenkov angle for nearly 200 rings which could be well-separated. Some events are also seen with two times more detected photons per ring than expected. They are due to Čerenkov radiation of an overlapping e^+e^- pair.*
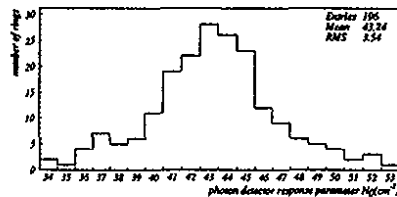

Figure 24: *The distribution of the photon detector response parameter N_0.*

References

[1] T. Lohse et al. Proposal for HERA-B, DESY PRC-94/02, May 1994.

[2] P. Križan, R. Mankel, D. Ressing, S. Shuvalov, M. Spahn, Nucl. Instr. Meth. in Phys. Res. A351 (1994) 111-131.

[3] J.L. Rosen, Nucl. Instr. Meth. in Phys. Res. A408(1998)191.

[4] S. Korpar et al., Nucl. Instr. and Meth. in Phys. Res. A433 (1999) 128-135.

[5] D. Dujmić, K. Reeves, HERA-B RICH Note 97-182, Hamburg 1997 HERA-B Note.

[6] T. Hamacher et al., Nucl. Instr. and Meth. in Phys. Res. A371 (1996) 289-294.

[7] P. Križan, M. Cindro, V. Cindro, S. Korpar, G. Omahen, A. Stanovnik, M. Starič, Nucl. Instr. and Meth. in Phys. Res. A364 (1995) 243-252.

[8] P. Križan, S. Korpar, M. Starič, A. Stanovnik, M. Cindro, D. Škrk, M. Zavrtanik, T. Hamacher and E. Michel, 1994 IEEE NSS Conference Record, Volume 2 (1995) 985-988.

[9] J. Pyrlik at al., Nucl. Instr. and Meth. in Phys. Res. A414 (1998) 170-181.

[10] S. Korpar, P. Križan, A. Stanovnik, M. Starič, D. Škrk, IEEE Transactions on Nuclear Science, Vol. 46, Number 3 (1999) 317-320.

[11] P. Križan, S. Korpar, M. Starič, A. Stanovnik, M. Cindro, D. Škrk, M. Zavrtanik, T. Hamacher, E. Michel, Nucl. Instr. and Meth. in Phys. Res. 371 (1996) 151-154.

[12] P. Križan et al., Nucl. Instr. and Meth. in Phys. Res. A387 (1997) 146-149.

[13] Hamamatsu Data Sheets for R5900-M16 and R5900-M4 Photomultipliers.

[14] J. McGill, R. Schwitters, HERA-B Note 96-278, DESY, Hamburg (1996); D. Broemmelsiek, Nucl. Instr. and Meth. in Phys. Res. A433 (1999) 136-142.

[15] R. Eckmann, M. Ispirian, S. Karabekyan, J. McGill, R. Schwitters, HERA-B Note 97-162, DESY, Hamburg (1997).

[16] F.M. Newcomer et al., IEEE Transactions on Nuclear Science, 40,4 (August 1993)630.

[17] P. Križan, M. Starič, Nucl. Instr. and Meth. in Phys. Res. A379 (1996) 124-129.

[18] R. Schwitters, HERA-B Note 97-088, DESY, Hamburg (1997); D. Dujmić, R. Schwitters, HERA-B Note 98-052, DESY, Hamburg (1998).

[19] J. Pyrlik and K. Lau, HERA-B Note 97-182, DESY, Hamburg (1997).

[20] P. Križan, S. Korpar, R. Pestotnik, M. Starič, A. Stanovnik, E. Michel, C. Oehser, W. Schmidt-Parzefall, A. Schwarz, T. Hamacher, D. Broemmelsiek, J. Pyrlik, Nucl. Instr. and Meth. in Phys. Res. **A394** (1997) 27-34.

[21] V. Cindro, S. Korpar, P. Križan, A. Stanovnik, M. Starič, D. Škrk, Nucl. Instr. and Meth. in Phys. Res. **A337** (1994) 609-612.

[22] S. Korpar, R. Pestotnik, P. Križan, IJS Report, IJS-DP-7615, Ljubljana (1997); HERA-B Note 97-079, DESY, Hamburg (1997).

[23] S. Korpar et al., Proc. of the 2nd Conference on Photodetection, Beaune, France, June 1999, to be published in Nucl. Instr. and Meth. in Phys. Res.

[24] S. Korpar et al., IJS Report, IJS-DP, Ljubljana (1999).

[25] D. Škrk, Doctoral thesis, Univerza v Ljubljani, Fakulteta za matematiko in fiziko, Oddelek za fiziko, Ljubljana, June 1999.

[26] R. Schwitters, HERA-B Note 99-215, DESY, Hamburg (1999).